International Journal of Non–Linear Mechanics 167 (2024) 104878

Contents lists available at ScienceDirect

International Journal of Non-Linear Mechanics

journal homepage: www.elsevier.com/locate/nlm

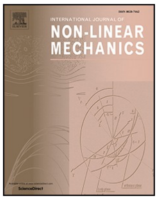

Vibration mitigation of a model aircraft with high-aspect-ratio wings using two-dimensional nonlinear vibration absorbers

Judith D. Brown [a], Manal Mustafa [a], Keegan J. Moore [b,*]

[a] Department of Mechanical and Materials Engineering, University of Nebraska-Lincoln, Lincoln, NE, 68588, USA
[b] Daniel Guggenheim School of Aerospace Engineering, Georgia Institute of Technology, Atlanta, GA 30332, USA

ARTICLE INFO

Keywords:
Nonlinear vibration absorber
Vibration mitigation
Commercial aircraft
High-aspect-ratio wings

ABSTRACT

High-aspect-ratio (HAR) airplane wings have higher energy efficiency and present an economical alternative to standard airplane wings. HAR wings have a high span and a high lift-to-drag ratio, allowing the wing to require less thrust during flight. However, due to their length and construction, HAR wings exhibit low-frequency, high-amplitude vibrations in both vertical (yaw axis) and longitudinal (roll axis) directions. To combat these unwanted vibrations, a two-dimensional nonlinear vibration absorber (2D-NVA) is constructed and attached to a model HAR-wing airplane to verify its effectiveness at reducing vibrational motion. The 2D-NVA design, which was presented in a previous study, consists of two low-mass, rigid bodies namely the housing and the impactor. The housing consists of a ring-like rigid body in the shape of an ellipse, while the impactor is a solid cylindrical mass which resides inside the cavity of the housing. The 2D-NVA is designed such that the impactor can contact the inner surface of the housing under both impacts and constrained sliding motion. The present study focuses on the use of the 2D-NVA to mitigate multiple modes of vibration excited by impulsive loading of a model airplane with HAR wings in both vertical and longitudinal directions. The effectiveness of a single 2D-NVA is investigated computationally using a finite element model of the model airplane. These results are verified experimentally and the performance of two 2D-NVAs (one on each wing) is also investigated. The contributions of this work are that: 1) the 2D-NVA alters the global response of the model aircraft by mitigating all relevant modes in both directions simultaneously; 2) a single 2D-NVA is optimal for mitigating motion in the vertical direction, while two active 2D-NVAs are optimal for the longitudinal direction; and 3) the performance of the 2D-NVA is robust to changes in the frequency content of the parent structure.

1. Introduction

Next generation commercial aircrafts designs will use high-aspect-ratio (HAR) and ultra-HAR wings installed on conventional fuselages. Such designs improve efficiency by reducing drag and increasing lift. For example, NASA's Subsonic Ultra-Green Aircraft Research (also known as SUGAR) aircraft employs an ultra-HAR wing that is braced to the fuselage using a truss [1,2]. Despite the additional stiffness introduced by the truss, the aircraft possesses multiple bending modes below 20 Hz that oscillate in both vertical (yaw axis) and longitudinal (roll axis) directions at relatively high amplitudes. Vibration absorbers are often used to mitigate large, unwanted oscillations. The traditional linear approach to vibration damping is the use of a passive tuned mass damper, which is a small mass tuned to a have a frequency close to the target mode. The installation of a passive tuned mass damper leads to splitting the targeted mode into two new modes of vibration that have lower amplitude than the original mode and two different frequencies, with one being higher and the other being lower than the original frequency of the target mode [3]. Recent work has extended the concept of a tuned mass damper to bands of frequencies through the creation of subordinate oscillator arrays [5–7]. Although subordinate oscillator arrays can reduce the motion of multiple modes, they cannot dissipate energy from any modes that reside outside of their band of influence. In addition to passive tuned mass dampers, semi-active variants have also seen widespread use and these are able to adapt as the frequency of a mode changes due to changes in the structure [4].

Although tuned mass dampers are effective when only a single mode is of interest, they are unsuitable for mitigating vibrations at multiple modes because they have a fixed frequency (i.e., tuned to the target mode). As a result, they can only mitigate motion at frequencies that are

---

* Corresponding author.
E-mail address: kmoore@gatech.edu (K.J. Moore).

https://doi.org/10.1016/j.ijnonlinmec.2024.104878
Received 21 September 2023; Received in revised form 5 April 2024; Accepted 19 August 2024
Available online 20 August 2024

close to their own, and they become ineffective if excited at a different frequency. As a result, nonlinear vibration absorbers (NVAs) have become a focus of research for vibration mitigation because they incorporate nonlinearities that render their frequencies adaptive based on the response of the primary structure. A popular NVA is the nonlinear energy sink [8,9], which is a low-mass attachment installed on a linear parent structure using an essential nonlinear stiffness (i.e., zero linear stiffness in theory or weak linear stiffness in practice). Typically, an NES includes a weak linear viscous damper in the coupling, but recent studies have considered nonlinear damping as well [10–12]. The effectiveness of an NES is due to an irreversible transfer of energy from the primary structure to the NES, resulting in a rapid dissipation of the energy of the system. One important limitation of NESs is that they tend to exhibit a limited amplitude range of applicability, where if the excitation exceeds a certain amplitude, the NES saturates and is unable to rapidly dissipate energy from the primary structure. Numerous types of NESs have been studied including polynomial nonlinearities [13–19], vibro-impact nonlinearities [20–28], and piecewise nonlinearities [29–35]. The performance of NESs for mitigating aeroelastic responses, such as flutter, has also been investigated [36–38].

Generally, NESs respond in a unidirectional manner, such that several devices are necessary to mitigate motion in multiple directions simultaneously. Recent research has investigated the use of a two-dimensional NES where geometric nonlinearity was considered in both the parent structure and the NES through the transverse deformation of springs and dampers [39]. The results demonstrated that the NES was effective at mitigating the motion of the primary structure; however, the analysis performed does not mimic the dynamic behavior of a HAR-wing aircraft because the primary structure was treated as a nonlinear system whereas HAR-wing aircraft exhibit primarily linear behavior. Inspired by this application, our previous research introduced a new two-dimensional NVA (2D-NVA) and demonstrated that the proposed design was suitable for mitigating vibrations in multiple directions simultaneously [40]. The previous study focused on the effectiveness of the proposed 2D-NVA for mitigating the vibrations of a multi-story, linear tower designed to oscillate in two directions. In that system, the 2D-NVA was shown to effectively mitigate a single mode of vibration in each direction. The present research considers the same 2D-NVA system applied to a model HAR-wing aircraft exhibiting low-frequency vibrations in both the vertical and longitudinal directions. To maintain symmetry, one 2D-NVA is installed on each wing, and they can be configured in inactive and active states where an inactive 2D-NVA acts as additional mass to balance an active 2D-NVA on the other wing. The contributions of this work are that: 1) the 2D-NVA alters the global response of the model aircraft by mitigating all relevant modes in both directions simultaneously; 2) a single 2D-NVA is optimal for mitigating motion in the vertical direction, while two active 2D-NVAs are optimal for the longitudinal direction; and 3) the performance of the 2D-NVA is robust to changes in the frequency content of the parent structure. The first contribution is demonstrated by extracting the response of each mode from the simulated and measured signals using the inverse wavelet decomposition (IWD) [41], which is a novel signal decomposition method based on the inverse wavelet decomposition. The second contribution is shown experimentally where the performance of two active 2D-NVAs is found to be worse in the vertical direction, but better in the longitudinal direction. The third contribution is demonstrated experimentally where the natural frequencies of the aircraft are different in the configuration with one active and one inactive 2D-NVA and the configuration with two active 2D-NVAs. Specifically, the inclusion of an inactive 2D-NVA introduces additional mass to the aircraft, which causes the natural frequencies to decrease significantly in this configuration. In the case of two active 2D-NVAs, neither of the NVAs introduce mass effects and the natural frequencies of the aircraft remain similar to those without any attachments installed. The present research presents the first step towards investigating the performance of the 2D-NVA on aircraft response and focuses on impulsive loading. This type of loading could represent gust excitation or loads experienced during landing events. Future research is planned to investigate the performance of the 2D-NVA under aeroelastic loading for applications in flutter suppression.

The rest of this paper is divided as follows: Section 2 presents a description of the design of the model aircraft and the NVA. Section 3 focuses on a computational study of the performance of the proposed 2D-NVA system including the finite element (FE) model used for the airplane and the equations of motion for the 2D-NVA system. The mathematical model for the 2D-NVA includes the use of impulse-momentum theory for impact modeling and the method developed by Roithmayr [42,43] for the constrained sliding motion. Due to the complexity of the model, the computational study focuses on a single active 2D-NVA installed on the left wing while a second inactive 2D-NVA is installed on the right wing. The effectiveness of the 2D-NVA is investigated using the minimum force required for contact, the percent energy dissipated by different sources, and the 5% settling times. Section 3 closes with a presentation of the results of the computational study. Section 4 discusses the measurements and experimental study of the system for three configurations: first, the base linear configuration with no 2D-NVAs installed; second, one active 2D-NVA installed on the left wing and a second inactive 2D-NVA connected to the right wing; and third, one active 2D-NVA installed on each for two active total. The performance of the three configurations is compared using 5% settling times and maximum displacement amplitudes for both the vertical and longitudinal directions. The paper is finished with concluding remarks in Section 5.

2. The model HAR-wing aircraft and nonlinear vibration absorber

2.1. Model HAR-wing aircraft

For this work the model shown in Fig. 1 is used as the basic model for the HAR aircraft. It consists of a rectangular aluminum tube for the fuselage, two aluminum L-brackets, and two narrow aluminum beams for the wings. The model HAR-aircraft was designed to mimic the vibrations of real HAR-wing aircraft such as the SUGAR truss-braced wing aircraft [1,2] to study the effectiveness of the proposed NVA. The fuselage is constructed out of a rectangular tube with width and height of 0.1524 m, length of 0.6096 m, and a thickness of 0.00635 m. The L-brackets are 0.03175 m wide, 0.0508 m long, and 0.00632 m thick, and are used to couple the wings to the fuselage. The wings have a width of 0.0254 m, a thickness of 0.00635 m, and length of 1.212 m. The wings are swept at an angle of 35° resulting in a wingspan of 2.162 m. The wings have a mass of 0.6 kg each, the fuselage a mass of 5.9 kg, and the brackets have a mass of 0.049 kg each. Each wing is bolted to the L-brackets using four 10–32 UNF bolts and four #10 washers, adding an additional mass of 0.031 kg. Each bracket is bolted to the fuselage using two 1/4″-20 UNC bolts and two 1/4″ washers, adding an additional mass of 0.039 kg. Finally, four 5/16″-18 UNC eyebolts are installed on the top of the fuselage, which increase the total mass by 0.105 kg of mass. The combined total mass of the plane is 7.373 kg.

2.2. Design of the proposed nonlinear vibration absorber

We consider the dynamics of the 2D-NVA proposed in Ref. [40] when installed centered on the tip of the wing. A CAD model and a schematic representation of the2D-NVA are presented in Fig. 2a and b, respectively. As shown in Fig. 2b, the motion in the y-direction corresponds to the vertical motion of the plane and the z-direction to the longitudinal motion of the plane. The 2D-NVA consists of a housing, a ring-like rigid body, and a particle (or rigid body) called the impactor that resides inside the housing. The housing and the impactor are both coupled to the wing tip using linear springs and viscous dampers; however, they are independent of each other and don’t have direct coupling. Instead, they

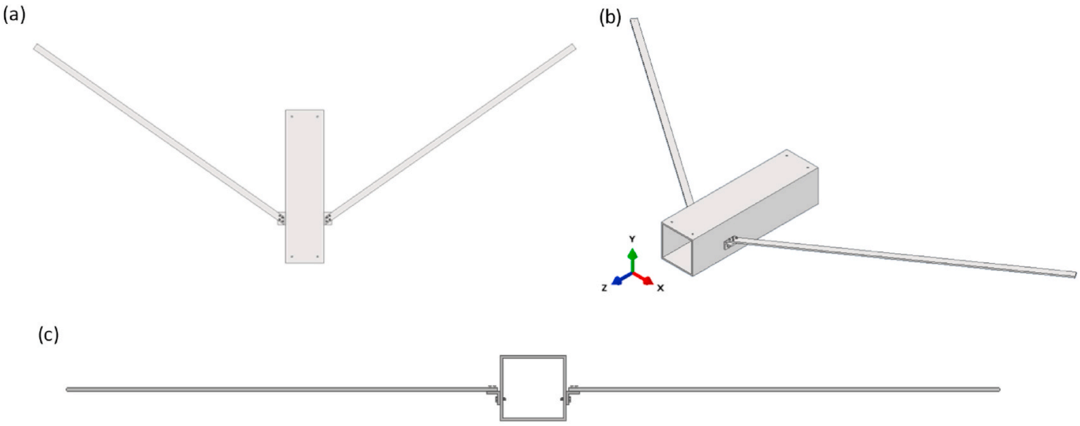

Fig. 1. CAD model of the model HAR-wing aircraft considered in this work showing (a) the top view, (b) orthographic view, and (c) the front view.

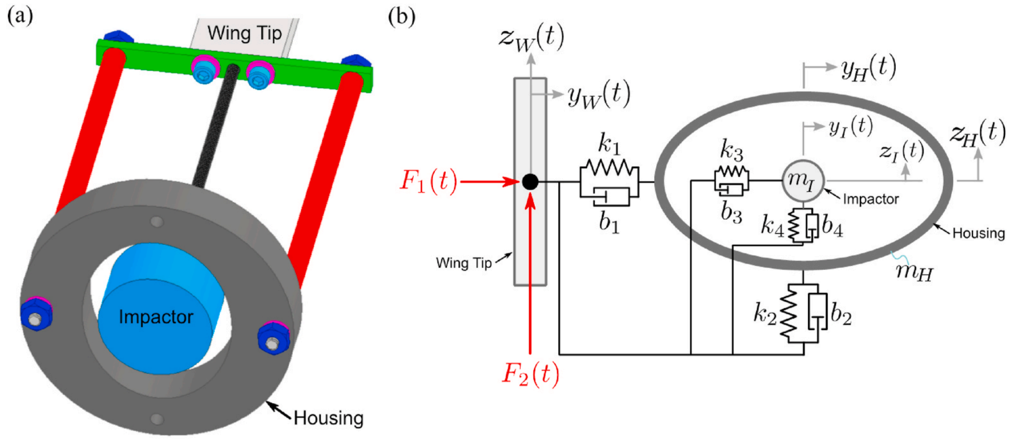

Fig. 2. (a) CAD model of the proposed 2D-NVA and (b) schematic representation of the proposed 2D-NVA connected to the center of the wing tip.

interact with each other through contact in the form of impacts and constrained frictional sliding motion when the excitation of the system is large enough. The interior cavity of the housing has the shape of an ellipse with major and minor radii of e_1 and e_2, such that its shape is defined as

$$\left(\frac{y}{e_1}\right)^2 + \left(\frac{z}{e_2}\right)^2 = 1, y \in [-e_1, e_1], z \in [-e_2, e_2]. \tag{1}$$

In the physical realization of the proposed 2D-NVA (illustrated in Fig. 2a), the housing is constructed using an Delrin® Acetal Resin disk with thickness of 0.0127 m, outer diameter of 0.0762 m, and an ellipse cut out of its center with major and minor radii of 0.0259 m and 0.0208 m, respectively. The housing is coupled to the wing using a mounting plate with two aluminum mounting posts with an active length of 0.1080 m and diameter of 0.00635. The mounting posts are attached to the housing and the mounting plate using 6–32 UNC threaded ends and corresponding nuts and washers. The impactor is constructed using a steel disk of thickness 0.0191 m and diameter of 0.03175 m and is connected to the wings using a nylon threaded rod with 6–32 UNC threads. The mounting plate is made from 6061 aluminum and has a length, width, and thickness of 0.0762 m, 0.00635 m, and 0.003175 m, respectively. The mounting plates are bolted directly to each wing using two 6–32 UNC bolts and corresponding washers. The housing and impactor have masses of 0.051 kg and 0.119 kg, respectively. The mounting plates including the hardware each have a mass of 0.006 kg, whereas the aluminum posts each have mass of 0.012 kg. Due to the shape of the impactor, the clearances in the vertical and longitudinal directions are smaller than the major and minor radii of the ellipse. Instead, these are $e_1 = 0.01003$ m and $e_2 = 0.00493$ m, such that $e_1 \approx 2e_2$. This design was selected because the first longitudinal mode of the plane has a frequency higher than the first vertical mode (see Section 3), such that motion in the longitudinal direction is expected to be smaller in amplitude than in vertical direction [44]. As a result, the smaller clearance allows for the 2D-NVA to be activated in the longitudinal direction for smaller displacements, such that it should effectively mitigate the longitudinal vibrations of the model HAR-wing plane.

3. Computational study

3.1. Finite element model for the model HAR-wing airplane

For the computational study, the airplane is modeled using finite elements using the software Abaqus®, and pictures of meshed assembly and parts are shown in Fig. 3. All parts are modeled using quadrilateral elements of type S4R. The fuselage has 1280 elements and 1312 nodes, the wings each have 368 elements and 423 nodes, and the brackets each have 270 elements and 304 nodes. The wings are coupled to the fuselage using two L-brackets with four fasteners on the wing side and 2 to fasten the fuselage and bracket. The mass of each bolt was incorporated as a lumped mass at the location of the bolt head in the physical system (see Fig. 1). The eyebolts were added as lumped masses to discrete points at their respective locations and these points were rigidly coupled to a region corresponding to the bolt holes. The use of fasteners couples a circular region around a central point (the bolt holes in this case) defined by the radius of influence. The type of connection defines how the regions on the two parts interact with each other. For simulation purposes

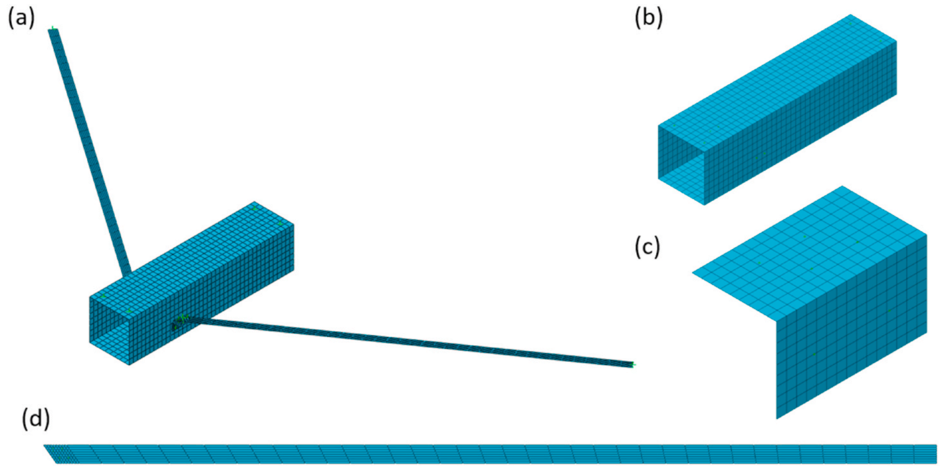

Fig. 3. The FE model for the model HAR airplane used in the computational study showing (a) the assembled system, (b) the mesh for the fuselage, (c) the mesh of the brackets, and (d) the mesh for the wings.

the connections were defined as rigid multi-point constraints, which rigidly couple the regions defined by the radii of influence together. The radius of influence for the fasteners coupling the wings to the L-brackets is 0.0055 m and that for the fasteners coupling the L-brackets to the fuselage is 0.00476 m.

The radii of influence were adjusted to minimize the error between the natural frequencies measured experimentally for the plane without any attachments and the FE model. The natural frequencies of the experimental plane were determined from free-response measurements for the plane as shown in Fig. 14a, except without any attachments installed. A comparison of the natural frequencies of the first six flexible modes between the experiment and FE model is provided in Table 1. The first two bending modes with dominant motion in the vertical direction are shown in Fig. 4a and b while the first two bending modes with dominant motion in the longitudinal direction are presented in Fig. 4c and d. The corresponding damping ratios were determined from the experimental frequency response function (FRFs) using the MFDID toolbox [45] and these are also provided in Table 1. The use of multi-point constraints and lack of friction is justified for the bolted joints because these joints are located at the roots of the wing, such that any relative displacements across them are small. As such, the effects of friction are expected to be weak and are captured on average by using damping ratios identified from the experimental measurements.

To enable extended simulations of the response of the model airplane, substructuring in Abaqus® was employed to create a reduced-order model using static and free-interface mode. The proposed model consists of the nodes at the center of each wing tip as well as the first 15 flexible modes. All six degrees-of-freedom (DOFs) at the two nodes are kept in the reduction, such that the reduced-order model has a total of 27 DOFs. The remaining physical nodes are used to couple the 2D-NVAs to the wing(s). A detailed description of the coupling procedure is discussed in the next subsection. The resulting first six natural frequencies of the reduced-order model presented in Table 1 are equal to the ones found for the full model. Thus, the developed reduced-order model can be considered as an adequate representation of the dynamics of the full-order model while enabling simulations of the response over long periods of time with minimal computational expense.

Table 1
Natural frequencies of the first six bending modes for the experimental system and FE models, and the corresponding damping ratios identified using experimental modal analysis and the MFDID toolbox [45].

#	Type	Exp. Freq. [Hz]	Full FE Model Freq. [Hz]	Reduced FE Model Freq. [Hz]	Reduced Model and 1 Inactive 2D-NVA [Hz]	Damping Ratio
1	Vertical	4.57	4.57	4.57	3.76	0.00360
2	Vertical	9.69	9.71	9.71	8.24	0.00242
3	Longitudinal	13.1	13.1	13.1	9.54	0.00132
4	Vertical	22.0	22.3	22.3	19.0	0.00092
5	Longitudinal	25.7	23.4	23.4	19.6	0.00082
6	Mixed	26.9	27.5	27.5	23.5	0.00075

3.2. *The governing equations of motion*

When the impactor and housing are not in contact, the dynamics of the system is entirely linear. The equations of motion governing the housing DOFs are

$$m_H\ddot{y}_H + b_1(\dot{y}_H - \dot{y}_w) + k_1(y_H - y_w) = 0, \tag{2a}$$

$$m_H\ddot{z}_H + b_2(\dot{z}_H - \dot{z}_w) + k_2(z_H - z_w) = 0, \tag{2b}$$

where $y_H(t)$ and $z_H(t)$ are the displacements of the housing in the vertical and longitudinal directions, respectively, and $y_w(t)$ and $z_w(t)$ are the displacements of the wing tip in the vertical and longitudinal directions, respectively. The equations of motion governing the impactor DOFs are

$$m_I\ddot{y}_I + b_3(\dot{y}_I - \dot{y}_w) + k_3(y_I - y_w) = 0, \tag{3a}$$

$$m_H\ddot{z}_H + b_2(\dot{z}_H - \dot{z}_w) + k_2(z_H - z_w) = 0, \tag{3b}$$

where $y_I(t)$ and $z_I(t)$ are the displacements of the impactor in the vertical and longitudinal directions, respectively.

The dynamics of the reduced FE model for the airplane when no NVAs are installed is represented by

$$M_p\ddot{u}_p + C_p\dot{u}_p + K_p u_p = F_p(t), \tag{4}$$

where $M_p, C_p,$ and K_p are the reduced mass, damping, and stiffness matrices produced by the FE model, $u_p(t)$ is the vector of nodal displacements and rotations and modal displacements. Finally, $F_p(t)$ represents the external excitation defined as

$$F_p(t) = \{0 \quad \cdots \quad 0 \quad F_1(t) \quad F_2(t) \quad 0 \quad \ldots \quad 0\}^T. \tag{5}$$

The forces $F_1(t)$ and $F_2(t)$ are applied to the vertical and longitudinal DOFs of the center of the wing tip as shown in Fig. 2 and are defined as

$$F_1(t) = P\cos\theta\sin\left(\frac{\pi}{T}t\right)(H(t) - H(t-T)), \tag{6a}$$

$$F_2(t) = P\sin\theta\sin\left(\frac{\pi}{T}t\right)(H(t) - H(t-T)), \tag{6b}$$

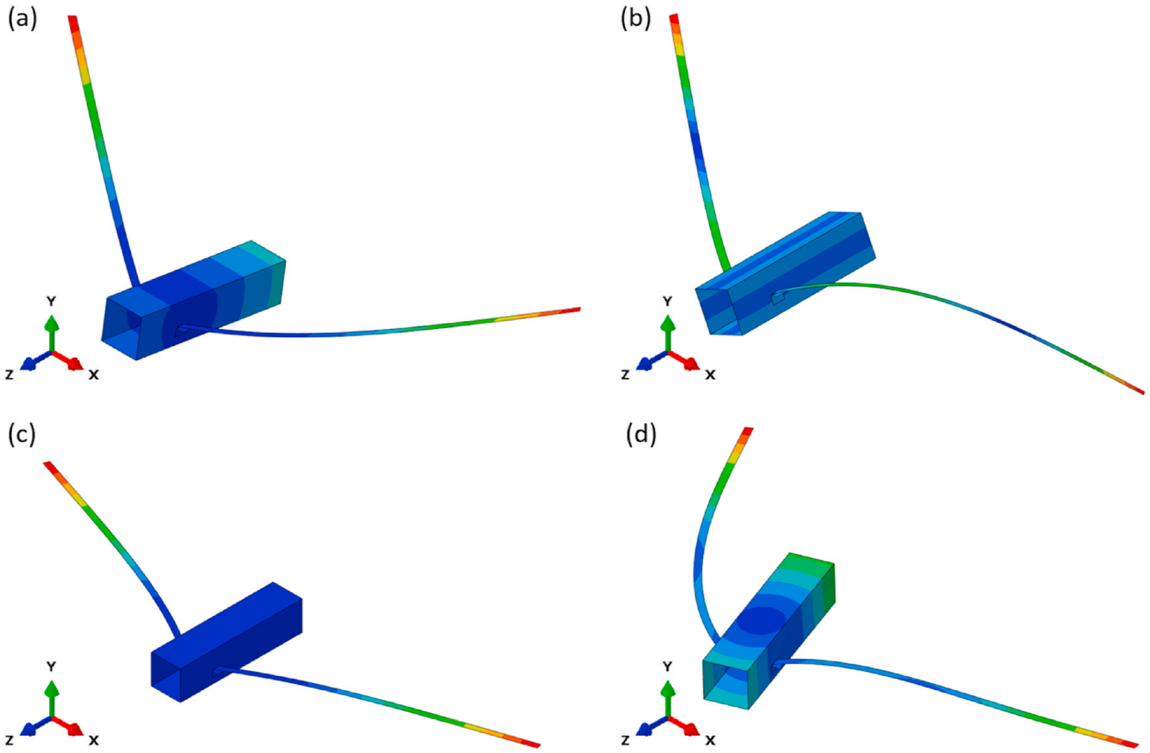

Fig. 4. Predicted mode shapes of the FE model for the model HAR-wing airplane with (a) and (b) showing the first two bending modes with dominant motion in the vertical direction (y-direction) and (c) and (d) showing the first two bending modes with dominant motion in the vertical direction (z-direction).

where $H(t)$ is the Heaviside function, T is the duration of the impulsive load, and the angle θ controls the direction of the applied force. The displacements of the wing tip are stored in the vector $u_p(t)$. The damping matrix is constructed using modal damping and the corresponding damping ratios are provided in Table 1. The damping ratios used are estimated using linear experimental modal analysis with the MFDID toolbox [45] and linear experimental measurements of the model airplane without the NVAs installed.

The installation of the 2D-NVA on the model airplane alters the dynamics of the system described by Eq. (4) to include the NVA dynamics and the resulting system is governed by the augmented system presented in Eq. 7 (a-c),

$$M\ddot{u} + C\dot{u} + Ku = F(t), \tag{7a}$$

$$M = \begin{bmatrix} M_p & 0 \\ 0 & M_N \end{bmatrix}, C = \begin{bmatrix} C_p & C_{pN} \\ C_{pN}^T & C_N \end{bmatrix}, K = \begin{bmatrix} K_p & K_{pN} \\ K_{pN}^T & K_N \end{bmatrix}, F(t) = \left\{ F_p(t) \;\; 0 \;\; 0 \;\; 0 \;\; 0 \right\}^T, \tag{7b}$$

$$u = \left\{ u_p \quad y_H \quad z_H \quad y_I \quad z_I \right\}^T, \tag{7c}$$

where M_N, C_N, and K_N represent the mass, damping, and stiffness acting on the NVA DOFs, and C_{pN} and K_{pN} are the coupling damping and stiffness that connect the NVA to the wingtip of the model airplane.

Due to the complexity required to simulate the response of multiple 2D-NVAs, we consider the performance of a single active 2D-NVA installed on the left wing while an inactive 2D-NVA is installed on the right wing. The performance of multiple active 2D-NVAs is considered in the experimental study discussed in Section 4. The inactive 2D-NVA is incorporated by adding the mass of the housing and impactor directly to the DOFs of the right-wing tip and it acts to balance the mass introduced by the active 2D-NVA. The masses of the housing and impactor are equivalent to the experimental system and the mass of the two aluminum posts and mounting plate were added to the wingtip DOFs in the mass matrix of the FE model. Specifically, the mass of the inactive 2D-NVA consists of the housing, impactor, mounting plate, three aluminum posts (two for the housing and one for the impactor), and all associated hardware. For the active 2D-NVA, the lumped mass added to the wing includes two aluminum posts for the housing, mounting plate, hardware used to connect the posts to the mounting plate, and the hardware used to connect the mounting plate to the wing. The total mass added to the wing tip for the inactive 2D-NVA is 0.214 kg and for the active 2D-NVA the added mass is 0.03 kg. The inactive 2D-NVA increases the effective mass of the plane and causes the natural frequencies to decrease. We report the natural frequencies of the plane in this configuration in Table 1.

3.3. *Minimum energy for contact*

The minimum energy necessary for contact to occur between the impactor and housing is

$$E_{min} = \frac{1}{2}\min\left(k_3 e_1^2, k_4 e_2^2\right), \tag{8}$$

and the system responds linearly when the total energy below this minimum regardless of how the energy is distributed throughout the system. When the total energy is above this minimum, the dynamics of the system are only potentially nonlinear as the energy distributed to the housing and impactor could be too small to result in contact. We use the minimum energy described in Eq. (8) to split the simulation of the dynamics into two parts. First, if the total energy is above the minimum energy, we simulate the response using *ode113* in MATLAB®, which is a variable order method that is efficient at maintaining stringent tolerances. We use this solver to ensure that the times of contact are computed with minimal errors. When the mechanical energy is less than the minimum, integration is halted and the solver switches to *ode45* for the remainder of the simulation because the dynamics is purely linear and stringent tolerances are no longer necessary.

3.4. New initial conditions after impact

Using the ellipse equation from Eq. (1), we define the contact condition as

$$Q = \left(\frac{y_I - y_H}{e_1}\right)^2 + \left(\frac{z_i - z_H}{e_2}\right)^2, Q \in [0, 1], \tag{9}$$

where $Q = 1$ corresponds to contact between the housing and the impactor. Once contact occurs, the integration is halted, and the code computes new initial conditions using impulse-momentum theory. This is accomplished by transforming the impactor and housing velocities into normal and tangential coordinates as

$$v_{It}^- = \dot{y}_I^- \cos\phi + \dot{z}_I^- \sin\phi, \tag{10a}$$

$$v_{In}^- = -\dot{y}_I^- \sin\phi + \dot{z}_I^- \cos\phi, \tag{10b}$$

$$v_{Ht}^- = \dot{y}_H^- \cos\phi + \dot{z}_H^- \sin\phi, \tag{10c}$$

$$v_{Hn}^- = -\dot{y}_H^- \sin\phi + \dot{z}_H^- \cos\phi, \tag{10d}$$

where the subscripts "t" and "n" correspond to tangential and normal directions, respectively, the dash superscript " $-$ " implies that the velocities are taken right at the instant of contact. The angle ϕ is the angle between the horizontal and tangential directions and is computed as

$$\phi = \tan^{-1}\left(-\frac{e_2^2(y_I - y_H)}{e_1^2(z_I - z_H)}\right). \tag{11}$$

In this coordinate system, linear momentum is conserved in the tangential direction resulting in

$$v_{It}^+ = v_{It}^-, v_{Ht}^+ = v_{Ht}^-, \tag{12}$$

where the superscript " $+$ " indicates the velocities in the instant after the impact. The new velocities in the normal direction are computed using the solution to a one-dimensional collision, resulting in

$$v_{In}^+ = \frac{m_I v_{In}^- + m_H\left(v_{Hn}^- + \gamma\left(v_{Hn}^- - v_{In}^-\right)\right)}{m_I + m_H}, \tag{13}$$

and

$$v_{Hn}^+ = \frac{m_H v_{Hn}^- + m_I\left(v_{In}^- + \gamma\left(v_{In}^- - v_{Hn}^-\right)\right)}{m_I + m_H}, \tag{14}$$

where γ is the coefficient of restitution. The new initial velocities are then computed using the inverse transformation as

$$\dot{y}_I^+ = v_{It}^+ \cos\phi - v_{In}^+ \sin\phi, \tag{15a}$$

$$\dot{z}_I^+ = v_{It}^+ \sin\phi + v_{In}^+ \cos\phi, \tag{15b}$$

$$\dot{y}_H^+ = v_{Ht}^+ \cos\phi - v_{Hn}^+ \sin\phi, \tag{15c}$$

$$\dot{z}_H^+ = v_{Ht}^+ \sin\phi + v_{Hn}^+ \cos\phi. \tag{15d}$$

After the solving the collision problem, the relative normal velocity, $v_{In}^+ - v_{Hn}^+$, is computed and used to determine whether separation occurs after the impact or if the impactor and housing begin sliding against each other. Theoretically, the two will always separate unless the relative normal velocity is zero; however, this condition cannot be realized exactly due to small numerical errors and the need for integration time steps that are smaller than machine epsilon. To overcome this issue, we enforce sustained contact when

$$\left|v_{In}^+ - v_{Hn}^+\right| \leq 2 \times 10^{-4}\ \mathrm{m/s}, \tag{16}$$

which is small enough to ensure that the times between impacts remain larger than machine epsilon without computing excessive amounts of low-amplitude impacts. As such, in our numerical implementation, when Eq. (16) is satisfied, the simulation switches to solving a constrained dynamics problem that forces the impactor to slide along the inside surface of the housing. This problem is discussed in the next subsection. When Eq. (16) is not satisfied, the housing and impactor separate, and the numerical integration is continued based on the dynamics described by Eq. (7a).

3.5. Dynamics of the constrained sliding motion

When the condition described in Eq. (16) is satisfied, the code switches to computing the response of a constrained dynamics problem using the new initial velocities computed from the collision problem (i.e., Eq. 15). The method created by Roithmayr [42] is implemented to solve the constrained dynamics problem, which computes the constraint forces using a vector-based formulation. To explain this approach, we start by differentiating Eq. (9) once with respect to time to obtain the scaler form of the velocity constraint:

$$\frac{2(y_I - y_H)}{e_1^2}(\dot{y}_I - \dot{y}_H) + \frac{2(z_I - z_H)}{e_2^2}(\dot{z}_I - \dot{z}_H) = 0. \tag{17}$$

We then convert this into a vector form by letting $\dot{\boldsymbol{r}}_I = \dot{y}_I\hat{j} + \dot{z}_I\hat{k}$, $\dot{\boldsymbol{r}}_H = \dot{y}_H\hat{j} + \dot{z}_H\hat{k}$, where we use bold form to indicate vector quantities, $\hat{j}$ is the unit vector in the vertical direction, $\hat{k}$ is the unit vector in the longitudinal direction, and

$$\boldsymbol{W} = \frac{2(y_I - y_H)}{e_1^2}\hat{j} + \frac{2(z_I - z_H)}{e_2^2}\hat{k}, \tag{18}$$

such that

$$\boldsymbol{W}\cdot(\dot{\boldsymbol{r}}_I - \dot{\boldsymbol{r}}_H) = 0. \tag{19}$$

Differentiating this relation with respect to time results in the vector form of the acceleration constraint equation:

$$\boldsymbol{W}\cdot\left(\ddot{\boldsymbol{r}}_I - \ddot{\boldsymbol{r}}_H\right) + \frac{d\boldsymbol{W}}{dt}\cdot(\dot{\boldsymbol{r}}_I - \dot{\boldsymbol{r}}_H) = 0, \tag{20}$$

where

$$\frac{d\boldsymbol{W}}{dt} = \frac{2}{e_1^2}(\dot{y}_I - \dot{y}_H)\hat{j} + \frac{2}{e_2^2}(\dot{z}_I - \dot{z}_H)\hat{k}. \tag{21}$$

From Newton's second law of motion, the accelerations can be expressed as

$$\ddot{\boldsymbol{r}}_I = \frac{\boldsymbol{f}_I + \boldsymbol{C}_I}{m_I} \text{ and } \ddot{\boldsymbol{r}}_H = \frac{\boldsymbol{f}_H + \boldsymbol{C}_H}{m_H}, \tag{22}$$

where $\boldsymbol{f}_I$ and $\boldsymbol{f}_H$ are the vector forms of all the non-constraint forces acting on the impactor and housing, respectively, and $\boldsymbol{C}_I$ and $\boldsymbol{C}_H$ represent the constraint forces acting on them. Recognizing that the constraint force acting on the housing must be opposite and equal to the force acting on the impactor, we conclude that $\boldsymbol{C}_I = -\boldsymbol{C}_H$. Furthermore, due to the dot product in Eq. (20), the constraint forces only need to be parallel to $\boldsymbol{W}$, such that they can be expressed as

$$\boldsymbol{C}_I = \lambda\boldsymbol{W} \text{ and } \boldsymbol{C}_H = -\lambda\boldsymbol{W}, \tag{23}$$

Substituting Eqs. (22) and (23) into Eq. (20) and expanding results in

$$\lambda\left[\boldsymbol{W}^2\left(\frac{1}{m_I} + \frac{1}{m_H}\right)\right] + \boldsymbol{W}\cdot\left(\frac{\boldsymbol{f}_I}{m_I} - \frac{\boldsymbol{f}_H}{m_H}\right) + \frac{d\boldsymbol{W}}{dt}\cdot(\dot{\boldsymbol{r}}_I - \dot{\boldsymbol{r}}_H) = 0, \tag{24}$$

and solving for λ produces

$$\lambda = -\frac{\boldsymbol{W}\cdot\left(\dfrac{\boldsymbol{f}_I}{m_I} - \dfrac{\boldsymbol{f}_H}{m_H}\right) + \dfrac{d\boldsymbol{W}}{dt}\cdot(\dot{\boldsymbol{r}}_I - \dot{\boldsymbol{r}}_H)}{\boldsymbol{W}^2\left(\dfrac{1}{m_I} + \dfrac{1}{m_H}\right)}. \tag{25}$$

Since the constraint forces should only act to prevent penetration of the impactor into the housing, the constrained motion is sustained as long as the normal component of the constraint force acting on the impactor remains negative or equal to zero. The normal component of the constraint force acting on the impactor is computed as

$$N_I = -C_{Iy}\sin\phi + C_{Iz}\cos\phi, \tag{26}$$

and this requirement is expressed as

$$N_I \leq 0. \tag{27}$$

When $N_I > 0$, we set the constraint forces to zero, allowing the impactor to separate from the housing, then revert to the original numerical integration of the unconstrained system. Lastly, we also incorporate Coulomb friction between the impactor and housing, and this force is computed as

$$\boldsymbol{F}_f = \mu N_I \,\text{sgn}(v_{It} - v_{Ht})(\cos\phi\hat{i} + \sin\phi\hat{j}). \tag{28}$$

Note that the friction force acts only in the tangential direction, such that it does not affect the constraint forces and is neglected in their calculation [40].

3.6. Computational parameters

For the computational study, we consider the performance of the 2D-NVA using the parameters presented in Table 2. The stiffness and damping values for the housing and the impactor were determined by measuring the free response of each component as shown in Fig. 5a and b, respectively. Specifically, the frequency response function (FRF) for each component was computed using the measured displacement response and applied force. The rational fraction polynomial method [46] was used to identify the natural frequency and damping ratio from the experimental FRFs, which were then used to compute the linear stiffness and damping coefficients. Comparisons between the experimentally measured and model FRFs are provided in Fig. 5c. The coefficient of friction was sourced from McMaster-Carr [47], which supplied the Delrin® disks for the construction of the housing. The coefficient of restitution for Delrin® on steel was studied by King et al. [48] and was found to be dependent on the impact velocity. However, the coefficient varied from ~0.891 to ~0.953 with a mean value of 0.932, such that the overall dependence on velocity is relatively weak. Thus, implementing a velocity-dependent coefficient of restitution would result in only small changes to the predicted behavior and performance of the 2D-NVA compared to using a velocity-independent coefficient. To this end, we chose to use a velocity-independent coefficient of restitution with a value of 0.932 (the mean value from Ref. [48]). The forcing amplitude range, P, is chosen to provide a wide range of excitation amplitudes and the forcing duration, T, is comparable to the duration of an impulsive force applied using a modal hammer with a soft rubber tip. The range of the forcing angle, θ, is chosen to capture the full range of behavior and accounts for the symmetry in the system. Specifically, the behavior of the system for $\theta \in [0, 90]$ ° is equivalent to $\theta \in [90, 180]$ °, $\theta \in [180, 270]$ °, and $\theta \in [270, 360]$ ° due to the symmetry in the elliptical housing, such that the response only needs to be simulated for the one quadrant in the unit circle.

Table 2
Parameters used in the computational study.

Parameter	Value	Units	Parameter	Value	Units
m_H	0.053	Kg	b_3	0.110	Ns/m
m_I	0.119	Kg	b_4	0.110	Ns/m
m_{Post}	0.012	Kg	e_1	0.0103	m
m_{Mount}	0.006	Kg	e_2	0.0051	m
k_1	3477	N/m	γ	0.93	–
k_2	3477	N/m	μ	0.25	–
k_3	18.21	N/m	P	$[1, 1000]$	N
k_4	18.21	N/m	θ	$[0, 90]$	°
b_1	0.05	Ns/m	T	0.0025	s
b_2	0.05	Ns/m			

3.7. Results

Our first computational study focused on determining the minimum forcing for a given angle necessary for the impactor to engage the housing (i.e., the minimum forcing in each direction needed to engage the nonlinearity). To accomplish this, we only need to simulate the response of the plane with the 2D-NVAs installed but without the impacts or constrained sliding included in the model, then calculate the maximum value of the contact condition, Q, described by Eq. (9). Due to the impulsive nature of the excitation, contact will occur early in the response, such that we only need to compute the motion for a short duration. We chose a duration of 1 s for this study as this is more than three times the period of the first mode of the plane with added mass and provides adequate time for impacts to occur. Because the system is linear and non-proportionally damped, the response, in theory, can be computed analytically by solving the state-space representation using matrix exponentials and symbolic integration. However, in practice the resulting system matrix is a 62×62 square matrix and computing the response analytically is not feasible computationally due to limited computing resources (e.g., memory, limited precision, etc.).

Instead of computing the analytical solution, we opted to simulate the response of the linear system numerically for 1 s using *ode45* in MATLAB® for 1000 forcing values in the range from 25 to 45 N and for 1001 angles in the range from 0 to 90°. The minimum and maximum forcing values were determined based on the results observed in initial simulations of the entire system with impacts and constrained sliding. Using the simulated response, we determined the forcing and angle values where contact occurs using

$$B(v_0, \theta) = \begin{cases} 1 & R \geq 1 \\ 0 & R < 1 \end{cases}, R = \max_{0\leq t\leq 1} Q(P, \theta, t), \tag{29}$$

where B is a Boolean function that determines when contact occurs for values of P and θ. The result of this analysis is presented in Fig. 6 where the light (yellow) and dark (blue) regions indicate cases where contact occurs or not, respectively. From Fig. 6, it can be seen that the angle with the lowest force required for contact is $\theta = 90$ ° with a force of $P = 29.97$ N, which is expected because the impactor has to travel the least to hit the housing at this angle. A local minimum is observed for $\theta = 0$ ° with a force of $P = 33.83$ N needed for contact, which may appear surprising because the impactor must travel the furthest distance in this direction to engage the housing. However, at this angle the energy is concentrated in the vertical direction and the motion of the wings is maximized in this direction. The angle that requires the largest force for contact to occur is $\theta = 38.79$ ° with a force of $P = 40.02$ N. At this angle, the impactor must travel 0.014 m to engage the housing. The fact that $\theta = 0$ ° represents a local minimum whereas an angle of $\theta = 38.7$ ° represents the global maximum suggests that the shape of the interior cavity of the housing could be modified to ensure that contact occurs at the same force level for all angles. However, an investigation into the effect of the shape of the housing cavity is out of scope for the present work and will be explored in future work.

To investigate the effectiveness of the 2D-NVA system, we simulated the response for 2000 forcing amplitudes from 1 to 1000 N (i.e., ~0.5 N increments) and 2001 angles from 0° to 90°, which corresponds to 4,002,000 different combinations. Note that at a forcing amplitude of 1000 N and angles of 0° and 90°, the displacement amplitudes of the

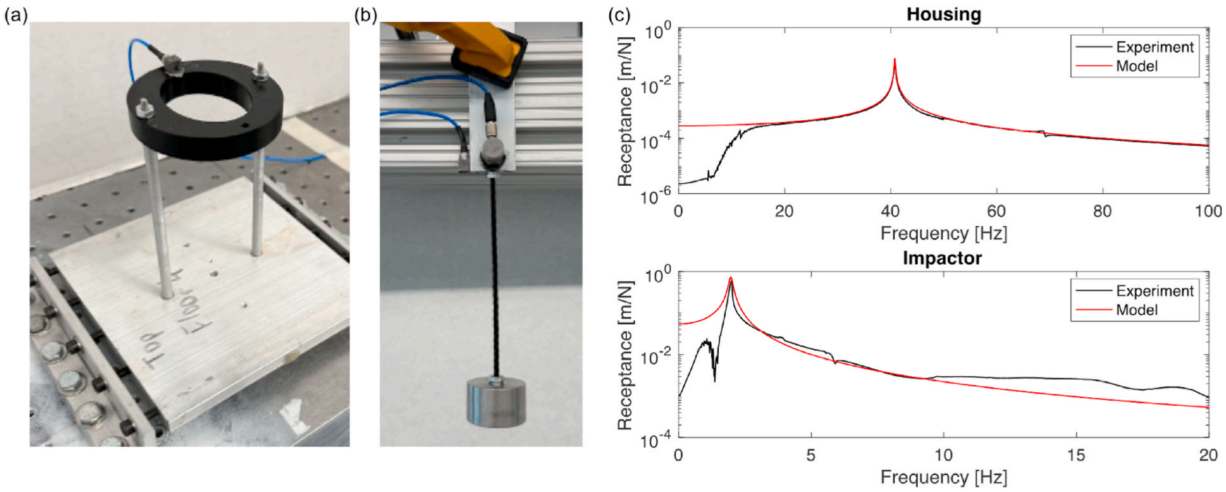

Fig. 5. The experimental setups used to measure and identify the linear dynamics of (a) the housing and (b) the impactor. (c) Comparisons of the experimentally measured and identified FRFs for the housing and impactor.

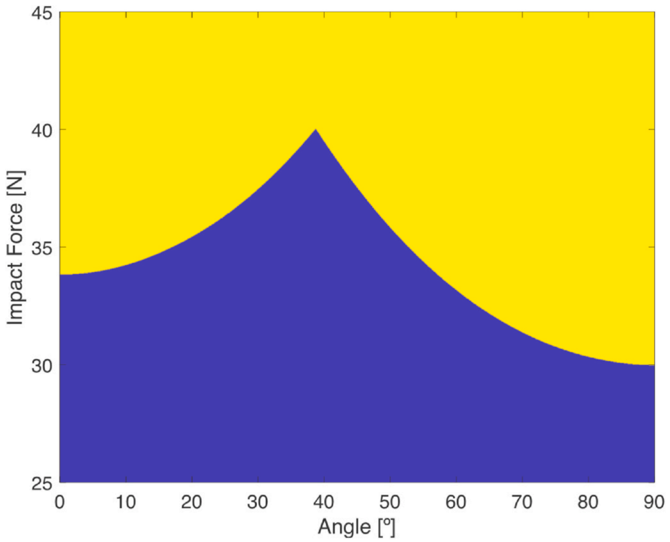

Fig. 6. The minimum impact force needed for contact to occur.

wings are on the order of 0.2 m and 0.08 m in the vertical and longitudinal directions, respectively. As such, such high forcing amplitudes may not represent physically realistic loading scenarios; however, simulating up to 1000 N allows us to investigate the potential limitations of the proposed 2D-NVA system. For all cases, we simulated the response for 64 s, which is long enough for the linear system to settle to 0.1% of the maximum displacement amplitude. For each simulation, we computed the 5% settling times of the vertical and longitudinal response of the wing tip with the active 2D-NVA as well as the percent energy dissipated by the damping of the plane, the housing and impactor dampers, impacts, and friction. We present the 5% settling times for the wing tip for the vertical and longitudinal directions in Fig. 7a and b, respectively. In general, the settling time in both directions are the highest inside the region where no contact occurs at low forcing amplitudes, and these times are on average 13.7 s in the vertical direction and 19.2 s in the longitudinal direction. The 5% settling times for the plane without any 2D-NVAs installed are 26.8 s and 22.6 s in the vertical and longitudinal directions, respectively. As such, for forces where the housing and impactor do not contact each other, the 2D-NVA reduces the 5% settling times of the plane by 48.7% in the vertical direction and by 15.0% in the longitudinal direction. For the region where contact occurs between the housing and impactor, the 5% settling times are on

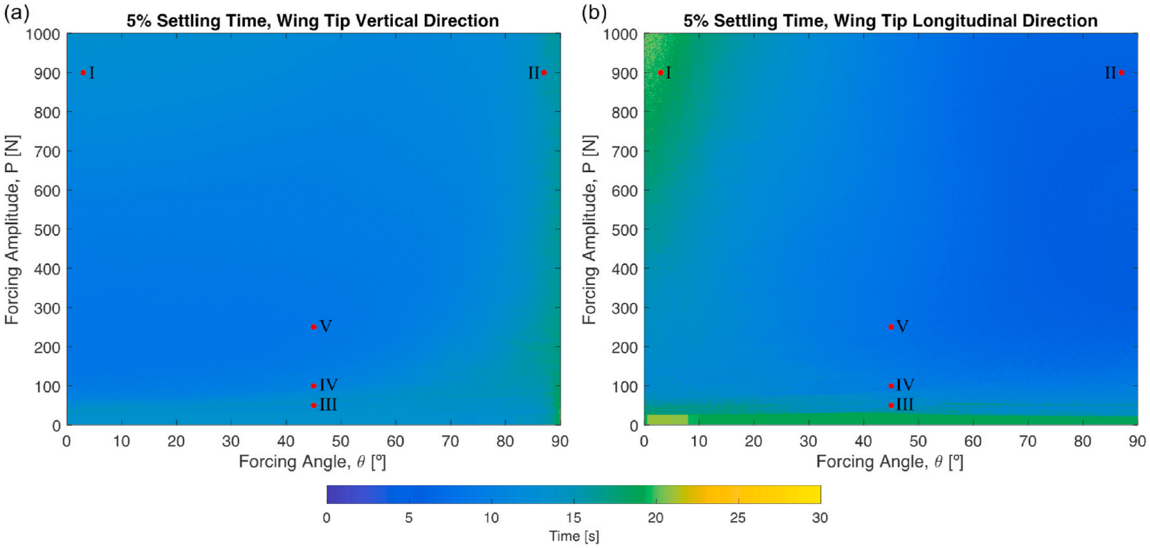

Fig. 7. The 5% settling times for the wing tip with one active 2D-NVA and one inactive 2D-NVA for (a) the vertical direction and (b) the longitudinal direction.

average 10.96 s and 9.8 s in the vertical and longitudinal directions, respectively, which correspond to a reduction of 59.1% and 56.6% compared to the settling times of the plane without any 2D-NVAs installed.

There is a band of higher settling times for the vertical direction around 90° and a similar band for the longitudinal direction around 0°. These bands arise because the energy, and therefore the resulting impacts, become concentrated in a single direction, such that the effectiveness of the 2D-NVA decreases in the other direction. For example, when θ approaches 90°, the energy in the system becomes concentrated in the longitudinal direction and the motion in the vertical direction is small, such that the 2D-NVA primarily mitigates motion in the longitudinal direction. To investigate this behavior, we consider the response of the left-wing tip for a forcing amplitude of 900 N and angles of 3° and 87° corresponding to points I and II on Fig. 7a and b, respectively. Starting with an angle of 3°, we present a comparison of the displacement responses and corresponding continuous wavelet transforms (CWTs) [49] for the vertical and longitudinal directions in Fig. 8a and b, respectively. Note that the displacement responses were high-pass filtered using a third-order Butterworth filter with a cutoff frequency 2.5 Hz to remove the rigid-body motion. The CWT provides a time-frequency representation of the signal content and the figures have been scaled such that darker shading corresponds to higher energy content at a particular time and frequency. Considering first the vertical displacement (Fig. 8a), the amplitude of the left wing with the 2D-NVA active is significantly smaller than that of the system without an NVAs installed. In fact, the maximum absolute displacement achieved by the wing without any NVAs installed is 0.205 m whereas it is only 0.074 m for the wing with the 2D-NVAs installed. Considering the CWTs, we find sets of horizontal bands that each represent a single component captured by the displacement response and correspond to a particular mode of the plane. The fact that the components do not change with time implies that they behave linearly despite the impacts and sliding incurred by the 2D-NVA. Moreover, the 2D-NVA mitigates not only the lowest mode in the vertical direction, but also the higher modes as well with mode 2 barely visible and modes 4 and 6 not appearing at all. Considering the longitudinal displacements, we find that on average the displacement amplitudes are comparable for both configurations of the system, except that the response with the 2D-NVAs at times exhibits a higher amplitude than the linear system. The CWT for the linear system (no 2D-NVAs installed) depicts a set of horizontal bands that correspond to the linear normal modes of the plane in the longitudinal direction. In contrast, the CWT for the nonlinear system (2D-NVAs installed) only contains horizontal bands after approximately 13 s of response. Before that time, the CWT depicts a chaotic region of mixed frequency content, which is caused by a strongly nonlinear transfer of energy facilitated by the impacts in the 2D-NVA. Specifically, the impacts of the 2D-NVA act as impulsive excitations for the longitudinal direction, such that energy is transferred from the vertical direction to the longitudinal direction through the 2D-NVA. This result implies that, for large forces, the 2D-NVA begins to saturate in terms of the amount of energy that it can dissipate, which is similar to the saturation phenomena observed in unidirectional NESs.

Considering now 900 N and 87°, we present the displacement response and corresponding CWT spectra of the left-wing tip for the vertical and longitudinal directions in Fig. 9a and b, respectively. Starting with the longitudinal response shown in Fig. 9b (because the forcing is primarily isolated to this direction at 87°), the amplitude of the linear response is nearly twice as large as that for the nonlinear case. In fact, the maximum absolute displacement achieved by the wing without any NVAs installed (the linear case) is 0.068 m whereas it is only 0.039 m for the nonlinear case. Moreover, the rate of dissipation in the case with the 2D-NVA installed is substantially larger than that of the underlying linear system. The CWT spectra reveal that modes 3 and 5 are both present in both the linear and nonlinear responses. However, in the nonlinear response, mode 5 is barely visible implying that it only contains a small amount of energy. The energy content in mode 3 is comparable for both simulations at the beginning, but this mode rapidly dissipates energy in the nonlinear case due to irreversible transfers of energy into the 2D-NVA. Moving on to the vertical response (Fig. 9a), we find that the displacement responses are comparable in amplitude like the longitudinal motion in the previous case. However, the CWT spectra reveal that the two responses are not similar. For the linear response, the CWT spectrum is populated by a set of horizontal bands representing modes 1, 2, 4, and 6, which all exhibit linear behavior as expected. For the nonlinear response, the CWT is populated by a scattering of energy

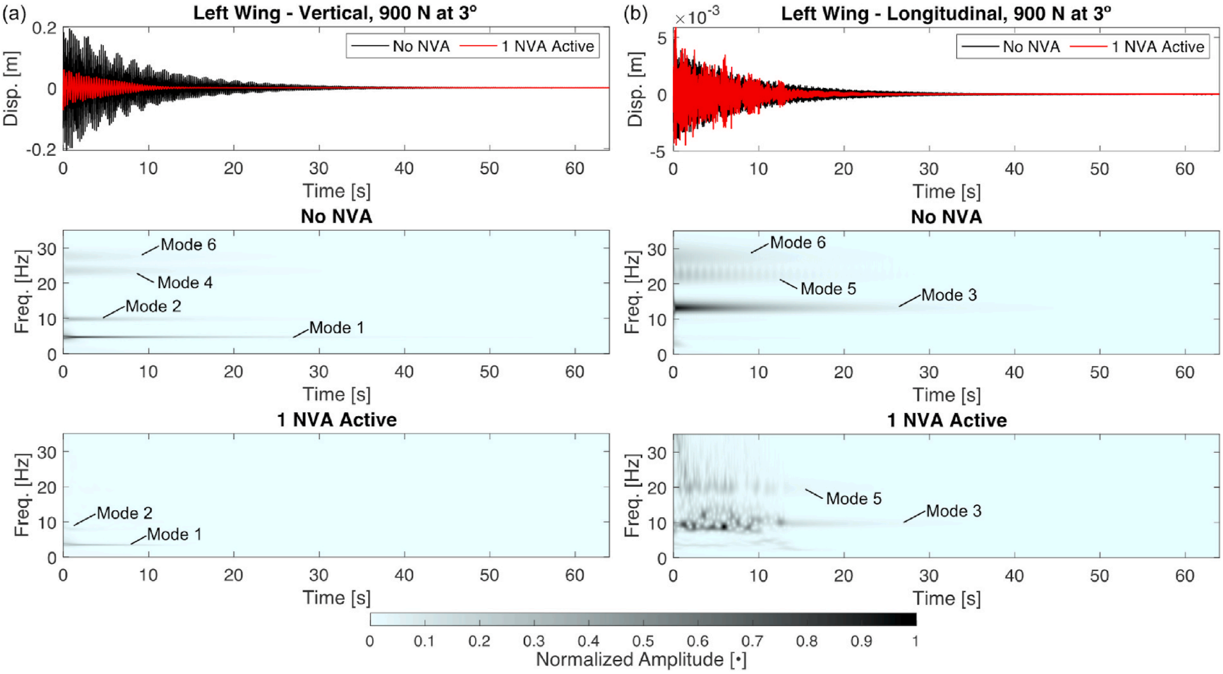

Fig. 8. Comparison of the displacement response and corresponding CWT spectra of the left-wing tip for 900 N at 3° for (a) the vertical direction and (b) the longitudinal direction.

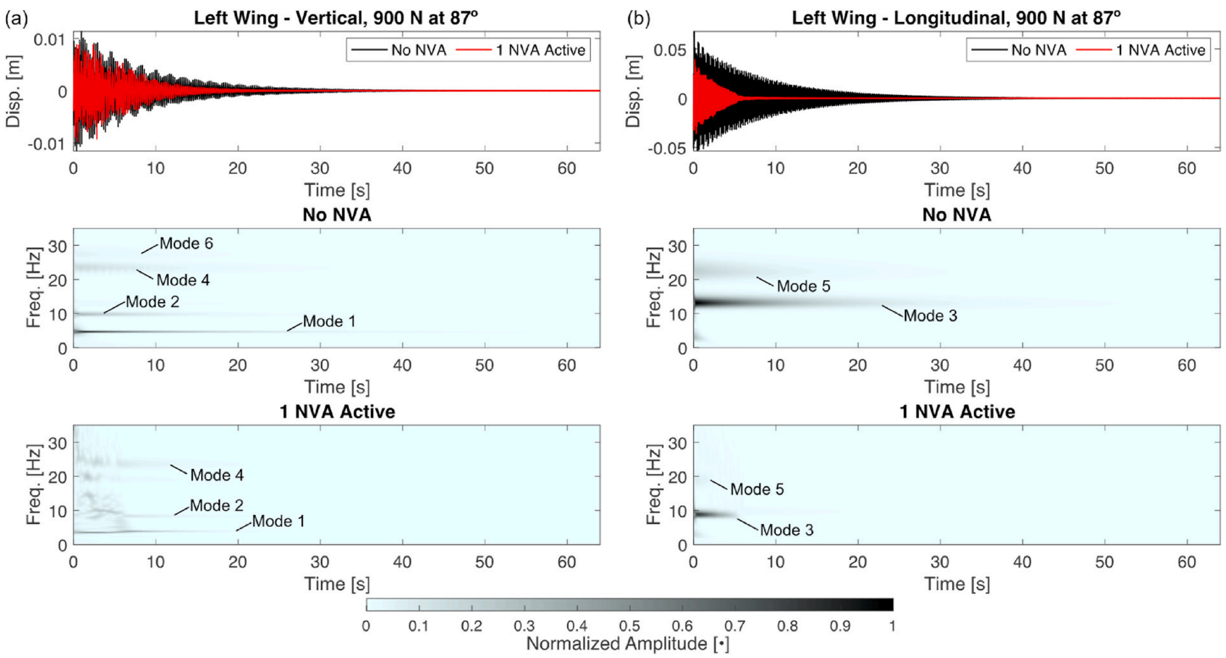

Fig. 9. Comparison of the displacement response and corresponding CWT spectra of the left-wing tip for 900 N at 87° for (a) the vertical direction and (b) the longitudinal direction.

across frequencies, which implies that energy is being injected into the vertical direction through the impacts that occur in the 2D-NVA. This behavior is like what was found for 900 N and 3° for the longitudinal direction and implies that the ability of the 2D-NVA to dissipate energy is beginning to saturate at this forcing level.

Fig. 10a through d provide insights into energy dissipation through the various components of the plane. Fig. 10a presents the percent energy dissipated by viscous damping of the model HAR airplane. This figure reveals that the damping of the plane plays only a small role in the dissipation of energy when the 2D-NVA is installed and active. In fact, for cases where no contact occurs between the housing and impactor (based on Fig. 6) the damping of the plane dissipates on average 35.7% of the total energy in the system whereas, for cases where contact does occur, the plane only dissipates 18.6% of the total energy. These averages were computed by partitioning the dissipated energies into regions corresponding to no contact and contact using the data shown in Fig. 6 and its inverse, then computing the respective mean values. As such, the damping of the plane plays only a small role in the dissipation of energy in the structure even for low forces where the nonlinearity of the 2D-NVA is not engaged. Fig. 10b depicts the percent energy dissipated by the viscous dampers associated with the 2D-NVA (i.e., the summation of the energy dissipated by the damper connected to the housing and the damper connected to the impactor). In the absence of contact, the dissipation is dominated by the linear viscous damping introduced by the active 2D-NVA, which dissipates on average 64.7% of the total energy, as seen in Fig. 10b. When contact does occur, the average energy dissipated by the 2D-NVA dampers decreases to 38.2%. Fig. 10c presents the percent energy dissipated by the inelastic impacts between the housing and the impactor and shows that the impacts dominate the dissipation of energy when they occur. In fact, when contact occurs, the impacts dissipate on average 41.8% of the total energy in the system. Finally, Fig. 10d depicts the percent energy dissipated for friction incurred due to impactor sliding along the interior surface of the housing. When contact occurs, friction is responsible for only 1.4% of the energy dissipated on average, such that the combined amount dissipated by nonlinear effects (i.e., impacts and friction) is 70.1%. Note that when contact does not occur, both impacts and friction dissipate exactly 0% of the total energy because there is no contact occurring between the housing and impactor.

To demonstrate that the 2D-NVA mitigates the motion of multiple modes of vibration simultaneously, we simulated the response of the linear and nonlinear systems for $\theta = 45\ ^\circ$ and $P = 50, 250,$ and 500 N (corresponding to points III, IV, and V on Fig. 7a and b, respectively), then decomposed the responses into separate components corresponding to each mode using the IWD method [41]. The IWD method acts as a filter by computing the inverse CWT for specified regions selected inside the CWT spectra, then extracting the corresponding time series for each region. Since the regions are chosen directly by the user, one can isolate specific components of the response (i.e., a specific mode), then extract a time series that corresponds to that specific component. To illustrate this approach, we depict the displacement responses and corresponding CWT spectra for $P = 50$ N in the vertical and longitudinal directions in Fig. 11a and b, respectively. The displacement responses show that the 2D-NVA is clearly able to mitigate the response in both directions simultaneously but does not provide insight into how the 2D-NVA affects each mode. To this end, we divide the CWT spectrum for each response into a set of regions that each correspond to a single mode as labeled in Fig. 11a and b. Note that the addition of an inactive 2D-NVA in the nonlinear case (labeled 1 NVA active) adds mass to the structure and reduces its natural frequencies. As such, the regions used to isolate individual modes are different for the linear and nonlinear systems and are chosen based on the underlying linear natural frequencies. Note that the IWD is not applied to the unlabeled regions in the CWT spectra as these regions do not capture the response of a mode of the plane. The same regions are used for all three forcing amplitudes considered because the natural frequencies of the plane do not change with the excitation amplitude or the energy in the system.

For the vertical direction, the IWD analysis results in four components corresponding to modes 1, 2, 4, and 6; however, to conserve space, we consider only the first and sixth modes in the analysis presented here. The justification for excluding the second and fourth modes is that if the 2D-NVA is effective at mitigating the sixth mode, which has the highest frequency of the modes considered in this study, then it will also mitigate the second and fourth modes. To this end, we depict the original displacement time series and the time series for the first and sixth modes in Fig. 12a, b, and c for $P = 50$ N, 100 N, and 250 N, respectively. In all

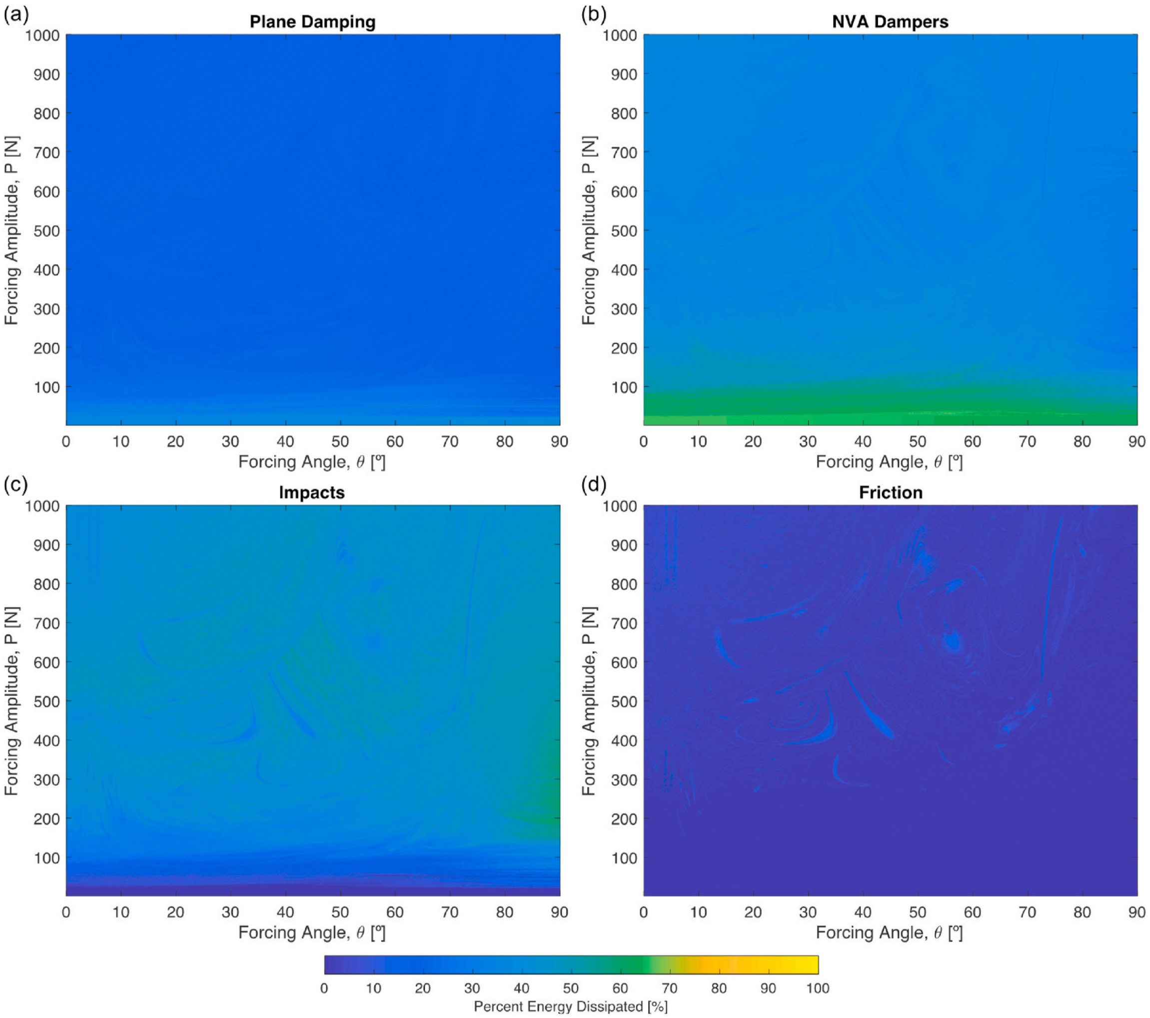

Fig. 10. The percent energy dissipated by (a) the damping of the plane, (b) the dampers of the active 2D-NVA, (c) impacts in the active 2D-NVA, and (d) friction caused by sliding in the active 2D-NVA.

three forcing cases, the amplitudes of the first and sixth modes of the plane with the 2D-NVAs installed are nearly half as large as those for the plane without any 2D-NVAs installed. This observation demonstrates that the ability of the 2D-NVA to minimize the amplitude of each mode does not change with the forcing amplitude at this angle; however, a clear change in the decay rates and trends is observed in both modes as the forcing amplitude increases.

For 50 N, both modes for the nonlinear system show an initially slow growth in amplitude before reaching a maximum and then decaying exponentially. This behavior is explained by the fact that both modes reach their maximum amplitudes around 1.2 s and the time of last impact occurs at 1.1806 s. As such, the impacts incurred by the 2D-NVA limit the maximum amplitude of both modes and after the impacts end, the linear damping of the mode takes over resulting in the exponential decay. For 100 N, the first mode for the nonlinear system does not exhibit an exponential decay at all whereas the sixth mode exhibits a lack of decay in the first 2 s followed by an exponential decay. In fact, during the first 2 s, the amplitude of the sixth mode oscillates with the peak amplitude remaining approximately constant, which indicates that it is receiving an infusion of energy due to the impacts of the 2D-NVA. This observation is verified by the fact that the final impact occurs at 2.2482 s (for this forcing level), which correlates to the time where the sixth mode begins to decay exponentially. As such, the 2D-NVA acts as a conduit for absorbing the energy from the first mode and scattering it to higher frequencies, such as the sixth mode. For 250 N, neither of the modes for the nonlinear system decay exponentially. Instead, the first mode exhibits a response that is comparable to that of a linear oscillator that is transferring energy into an NES [8]. This implies that the 2D-NVA is acting as a pure absorber for the first mode rather than as a conduit for transferring the energy of the first mode to higher modes. This observation is validated by the fact that the response of the first mode decays to near zero around 6 s and the time of the last impact is 5.7899 s, such that ceasing of the impacts is associated with the exiting of the first mode from the response of the plane. The response of the sixth mode reveals the presence of a beating pattern with the amplitude decreasing with time, which ceases around 6 s and gives way to exponential decay. Since the overall amplitude of sixth mode decreases during the first 6 s, the beating pattern is not caused by energy being transferred into it through the 2D-NVA. Instead, at this forcing level, the impacts in the 2D-NVA result in an exchange of energy between the sixth mode and the 2D-NVA itself, resulting in the beating pattern that is observed in the first 6 s.

For the longitudinal direction, the IWD analysis results in two components corresponding to modes 3 and 5, and we consider both modes in the analysis presented here. To this end, we depict the original displacement time series and the time series for the third and fifth modes in Fig. 13a, b, and c for $P = 50$ N, 100 N, and 250 N, respectively. In all three forcing cases, the amplitudes of the third mode of the plane with the 2D-NVAs installed are nearly half as large as those for the plane without any 2D-NVAs installed. A similar trend is found for the fifth

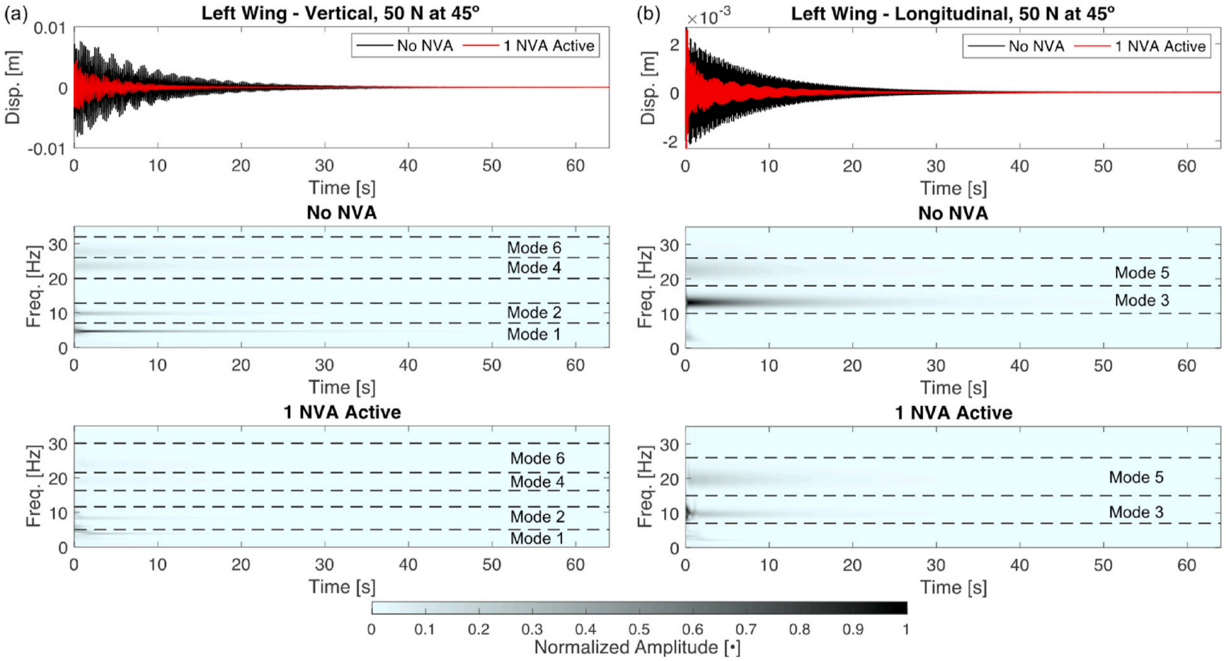

Fig. 11. Comparison of the displacement response and corresponding CWT spectra of the left-wing tip for 50 N at 45° for (a) the vertical direction and (b) the longitudinal direction.

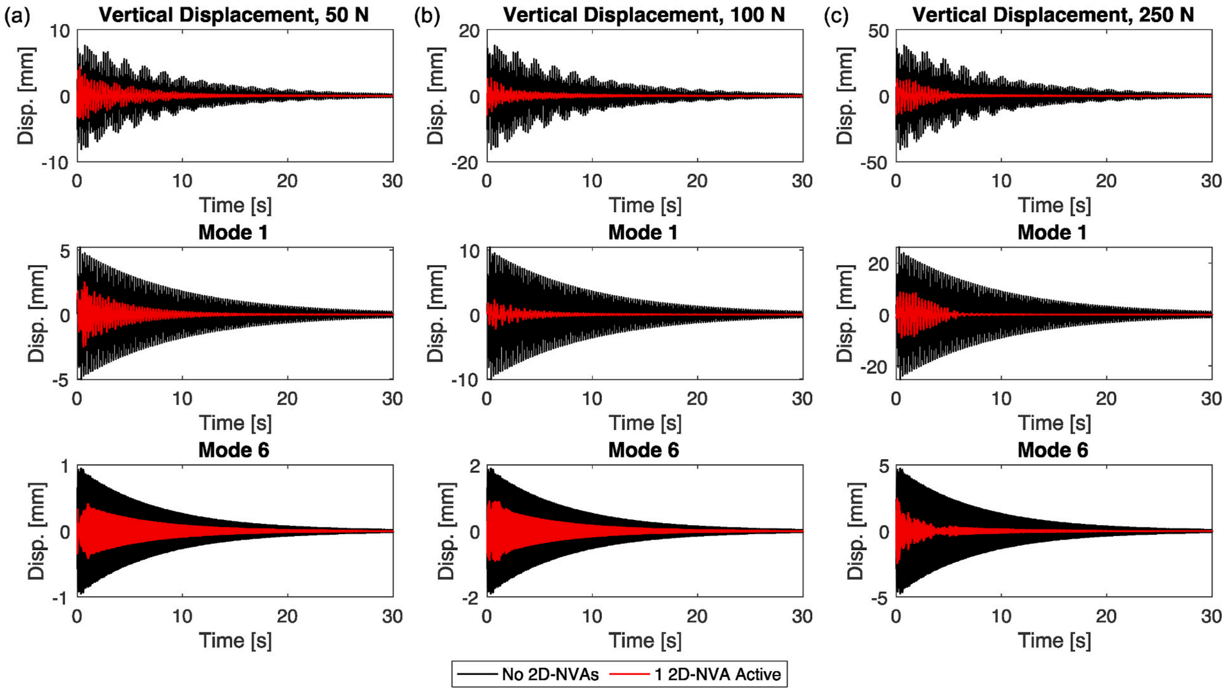

Fig. 12. The displacement response of the left-wing tip in the vertical direction and the responses of modes 1 and 6 for $\theta = 45$ ° and (a) $P = 50$ N, (b) $P = 100$ N, and (c) $P = 250$ N.

mode for 100 and 250 N; however, for 50 N, the response of the fifth mode is comparable for both configurations of the plane. Given this discrepancy, we assumed that there would be a threshold between 50 N and 100 N, where the 2D-NVA is suddenly able to mitigate the motion of the fifth mode. However, in searching for this threshold, we discovered that the 2D-NVA fails to mitigate the fifth mode only in the range of forcing amplitudes of [49.89, 50.004] N. As such, the failure of the 2D-NVA to mitigate the fifth mode for 50 N is coincidental and a result of the chaotic nature of the 2D-NVA due to the impacts. The first mode for 50 and 100 N and the fifth mode for 100 N exhibit non-steady decay rates in the beginning followed by exponential decays. The switching in decay trends in these cases corresponds to the ceasing of the impacts in the 2D-NVA exactly like the behavior observed for the vertical modes.

4. Experimental study

4.1. The experimental system and measurements

A picture of the experimental model HAR wing airplane is shown in Fig. 14a, which is suspended in a vertical configuration using two loops

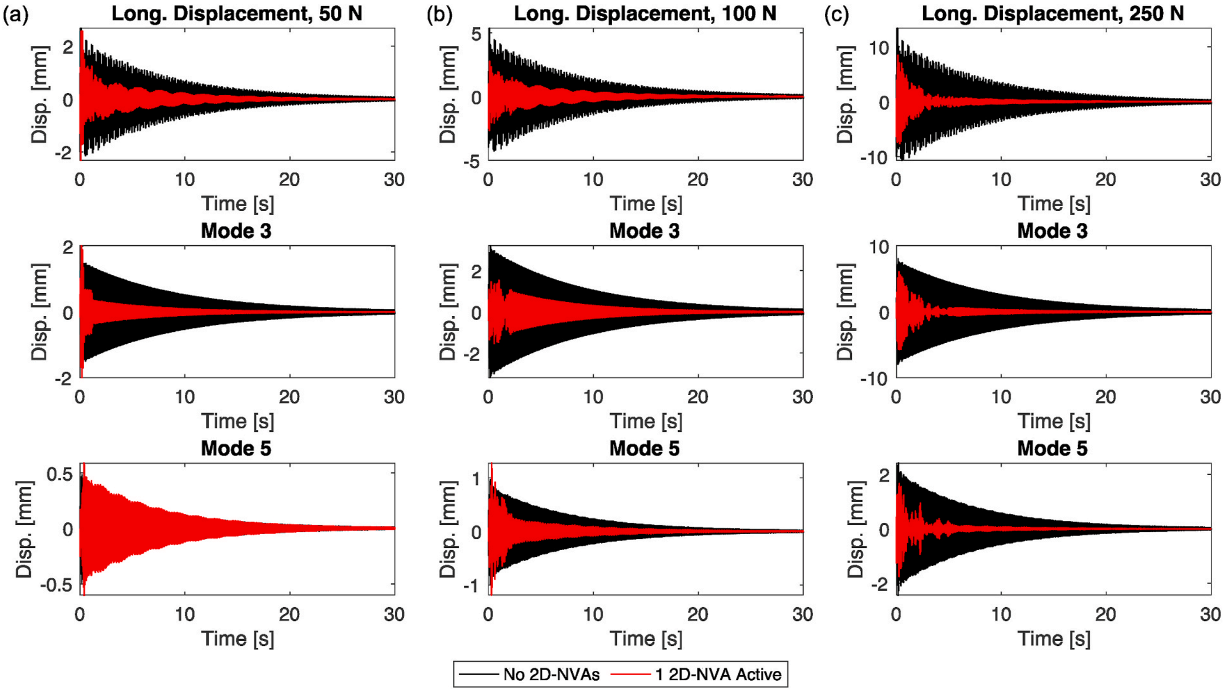

Fig. 13. The displacement response of the left-wing tip in the longitudinal direction and the responses of modes 3 and 5 for $\theta = 45\,^{\circ}$ and (a) $P = 50$ N, (b) $P = 100$ N, and (c) $P = 250$ N.

of fishing wire. Additionally, two bungees are connected to the front of the model airplane, and these were used to reduce the duration of the rigid-body modes (i.e., swaying motion). As depicted in Fig. 14a, the model airplane has one inactive 2D-NVA installed on the left wingtip and one active 2D-NVA installed on its right wingtip. Zoomed-in views of the inactive and active 2D-NVAs are provided in Fig. 14b and c, respectively. For the inactive 2D-NVA, the impactor is coupled to the wingtip using an aluminum rod, which introduces a strong linear stiffness and effectively acts as a rigid coupling at the frequencies of interest for the motion of the plane (i.e., below 50 Hz). The active 2D-NVA is achieved by coupling the impactor to the wingtip using a thin nylon rod that introduces a weak linear stiffness, such that the frequency governing the motion of the impactor is below the lowest frequency of the model airplane. In addition to the configuration shown in Fig. 14a, the response of the model airplane was also tested when no 2D-NVAs were installed on the wingtips, which we refer to as the nominal linear configuration, and when both 2D-NVAs were active.

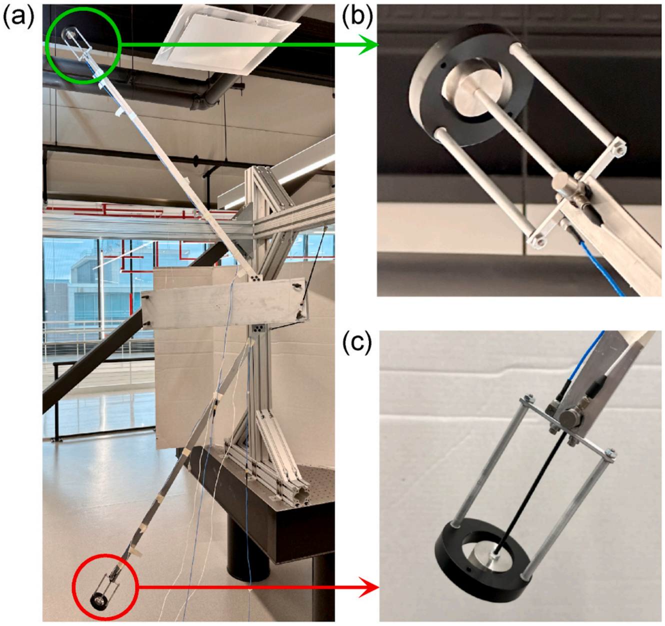

Fig. 14. (a) The experimental model HAR wing aircraft with one active and one passive 2D-NVA installed. (b) A zoomed-in view of the passive 2D-NVA where an aluminum rod is used to couple the impactor to the wingtip. The response of the wingtip is measured using the two accelerometers shown. (c) A zoomed-in view of the active 2D-NVA where a nylon threaded rod is used to couple the impactor to the wingtip.

The vertical response of each wingtip was measured using both a uniaxial accelerometer (PCB Piezotronics model 352C03, average sensitivity of 1.02 mV/(m/s^2)) whereas the longitudinal response of each wingtip was measured using triaxial accelerometer (PCB Piezotronics model 356A43, average sensitivity of 1.02 mV/(m/s^2)). Note that a coordinate transformation was applied to rotate the measured accelerations from triaxial accelerometers into the coordinate frame of the model airplane. The uniaxial accelerometers were used to measure the vertical response instead of the triaxial accelerometers because they have better noise performance at low frequencies and the lowest vertical mode occurs between 3.3 and 4.5 Hz depending on the configuration. In all cases, the model airplane was excited by applying an impulse to the left wingtip using a modal impact hammer (model 086C03), and the resulting transient response was measured for 60 s at a sampling rate of 16192 Hz using a Data Physics Abacus 906 data acquisition system and the Data Physics Software Suite (Data Physics, San Jose, CA, USA). The accelerations were then integrated numerically, and high-pass filtered using a third-order Butterworth filter with a cutoff frequency of 3 Hz to obtain the corresponding velocity response. This entire procedure was then applied to the velocities to obtain the displacement response in both the vertical and longitudinal directions.

4.2. *Effectiveness of the 2D-NVAs*

To validate the effectiveness of the 2D-NVAs, the response of the model airplane was measured for a range of forcing amplitudes in three configurations: no attachments installed, one active 2D-NVA and one inactive 2D-NVA, and two active 2D-NVAs. The model airplane was excited in the vertical and longitudinal directions separately for four different forcing amplitudes for each configuration.

Fig. 15a, b, c, and d present the response of the right wingtip in the vertical direction under vertical excitation at an amplitude of approximately 50, 75, 155, and 280 N, respectively, for all three configurations. Table 3 presents the 5% settling times for the described configurations under the forcing amplitudes chosen, as well as the calcuated time reduction percentages for the two configurations with active 2D-NVAs. The bottom row of Table 3 provides the average across all four forcing cases. The average settling time calcuated across all cases of the linear configuration is 11.89 s whereas with one 2D-NVA active the average is 2.36 s and with two active it is 2.27 s. Thus, we find that a single 2D-NVA introduces a dramatic reduction in the 5% settling time of the plane whereas the addition of a second active 2D-NVA does not. In fact, the average percent reduction for one active 2D-NVA is 80.2% whereas it is only 80.7% when two 2D-NVAs are active, resulting in an average increase of only 0.5%. This result is comparable to the results of [50] where the effects of two nonlinear stores were investigated on the global dynamics of a model experimental aircraft. Specifically, the results of [50] showed that the reduction in response of the aircraft when two nonlinear stores were active was nearly the same as the reduction when only one nonlinear store was active.

In addition to the decrement in the 5% settling time of the plane, the use of 2D-NVAs also led to a reduction the maximum vibration amplitude as seen in Fig. 15. To investigate this reduction, Table 4 presents the maximum displacement amplitudes for the three configurations across the used forcing amplitudes along with the percent reduction for the two cases with active 2D-NVAs. The bottom row of Table 4 provides the only averages of the percent reductions – the averages for the displacements are not computed because the displacement amplitudes are not comparable due to their dependence on the forcing amplitude unlike the 5% settling times. Considering first the reduction of amplitude caused by only one active 2D-NVA, we find that the percent reduction is quite consistent with an average of 66% reduction in amplitude and a standard deviation of only 2.40%. Surprisingly, the average percent reduction for the configuration with two active 2D-NVAs is less than that for only one active 2D-NVA, which is 5.5% less than that for only one active 2D-NVA, and the standard deviation is higher at 4.14%. In fact, the maximum displacement amplitude is higher for the case of two active 2D-NVAs than the case with only one active for all forcing amplitudes, such that the small gain in reduction of the settling time is overshadowed by the higher amplitude response. Based on these results, the configuration with only a single 2D-NVA active (with a second inactive 2D-NVA included as a counterweight) performs better than having two active 2D-NVAs at mitigating the vibrations in the vertical direction. However, it should be noted that the natural frequencies of the aircraft are different in the two configurations and the results demonstrate that the ability of the 2D-NVA to mitigate motion in the vertical direction is robust to changes in frequency.

Following the same procedure to assess the performance of the 2D-NVAs in the longitudinal direction, we present the response of the right wingtip in the longitudinal direction under longitudinal impact in Fig. 16a, b, c, and d for nominal forcing amplitudes of 50, 75, 165, and 250 N, respectively. Table 5 presents the 5% settling times for all three configurations for the four forcing amplitudes as well as the percent reduction for the two configurations with active 2D-NVAs. The bottom row of Table 5 presents the averages across the four forcing cases. The average settling time of the linear configuration is 9.55 s whereas for one active 2D-NVA it is only 3.6 s and for two active 2D-NVAs it is 3.65 s. Interestingly, we find that when two 2D-NVAs are active the average settling time actually increases compared to only one active 2D-NVA, but the difference is small enough that the performance of the two configurations is comparable. In fact, the average reduction in settling time is 62.4% for only one active 2D-NVA whereas it is 61.9% for two active 2D-NVAs, such that the addition of a second active 2D-NVA does not significantly change the behavior of the system. This result agrees with the results found for the vertical excitation. However, it should be noted that the natural frequencies of the aircraft are different in the two configurations and the results demonstrate that the ability of the 2D-NVA to mitigate motion in the longitudinal direction is robust to changes in frequency.

Similar to the vertical case, the 2D-NVAs reduced the maximum vibration amplitude in the longitudinal direction as seen in Fig. 16. To investigate this reduction, Table 6 presents the maximum displacement amplitude for the three configurations and the forcing amplitudes applied along with the percent reduction for the two cases with active 2D-NVAs. The bottom row of Table 6 provides the only averages of the percent reductions – for the same reasonning explained in the vertical case. For the configuration with only one active 2D-NVA, the average percent reduction in the displacement amplitude is only 37.4% whereas in the case of two active 2D-NVAs, the average percent reduction is considerably higher at 52.2%. Thus, unlike the 5% settling times or the performance in the vertical direction, using two active 2D-NVAs significantly reduced the displacement amplitude in the longitudinal direction as compared to the reduction caused by only one active 2D-NVA. Despite the increased reduction in displacement amplitude, the overall results suggest that using either one or two active 2D-NVAs is effective at mitigating the vibrations of the model HAR-wing airplane.

Although the clearance is smaller in the longitudinal direction (such that less energy is needed for the impactor to engage the housing), the experimental results show that the 2D-NVA is more effective in the vertical direction than in the longitudinal direction. For instance, the average percent reduction in the 5% settling time for one active 2D-NVA in the vertical direction is 80.2% compared to only 62.4% in the longitudinal direction for the same configuration. For the same configuration, the average percent reduction in displacement amplitude is 66.0% in the vertical direction compared to only 37.4% in the longitudinal direction. This observation suggests that further optimization of the interior of the shape of the housing could result in increased performance in the longitudinal direction while maintaining the performance in the vertical direction. Since the previous discussion in this section concluded that using only a single active 2D-NVA is optimal for mitigating the motion of this airplane, the interior shape could be optimized computationally using the numerical model discussed in Section 3, provided that the FE model is updated using the linear experimental results.

To demonstrate that the 2D-NVA mitigates the motion of multiple modes of vibration simultaneously, we apply the same IWD analysis as was used in studying the computational system. To this end, we present the displacement response and corresponding CWT spectra for 50 N of the right wing for the vertical and longitudinal directions in Fig. 17a and b, respectively. Given the correspondence between the linear FE model and the experimental structure (as discussed in Section 3.1.), the CWT spectra can be divided into the same regions as those used in the computational study to extract the first six modes of the plane. The regions considered in this analysis and the modes that they correspond to are depicted in the CWT spectra shown in Fig. 17a and b. Note that, in the case of the two active 2D-NVAs, the modes of the plane have

Table 3
The 5% settling times for vertical response under vertical excitation.

Force [N]	No NVAs	One 2D-NVA Active		Two 2D-NVAs Active	
	Time [s]	Time [s]	Percent Reduction [%]	Time [s]	Percent Reduction [%]
50	12.48	3.46	72.3	2.13	82.9
75	9.83	1.96	80.1	2.12	78.4
155	12.11	1.59	86.9	2.56	78.9
280	13.12	2.41	81.6	2.27	82.7
Average	**11.89**	**2.36**	**80.2**	**2.27**	**80.7**

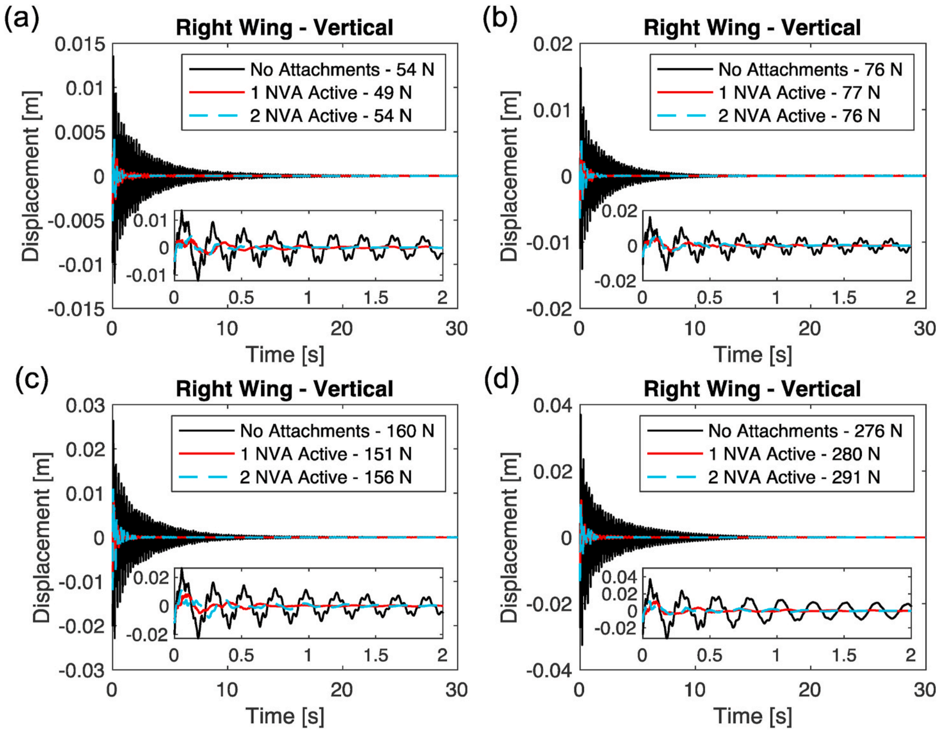

Fig. 15. The vertical response of the right wingtip for the three configurations under impulsive excitation in the vertical direction with nominal amplitude of (a) 50 N, (b), 76 N, (c) 155 N, and (d) 280 N.

Table 4
The maximum displacement for vertical response under vertical excitation.

Force [N]	No NVAs	One 2D-NVA Active		Two 2D-NVAs Active	
	Displacement [mm]	Displacement [mm]	Percent Reduction [%]	Displacement [mm]	Percent Reduction [%]
50	13.51	4.45	67.1	5.12	62.1
75	16.26	6.04	62.9	6.42	60.5
155	26.38	9.11	65.5	11.93	54.8
280	37.03	11.68	68.5	13.14	64.5
Average	-	-	**66.0**	-	**60.5**

comparable frequencies to those of the plane without any attachments. Thus, we used the same regions for the IWD analysis for the case of no NVAs installed and the case of two active 2D-NVAs. Just as in the computational study, the IWD is not applied to the unlabeled regions in the CWT spectra as these regions do not capture the response of a mode of the plane. The same regions are used for all three forcing amplitudes considered because the natural frequencies of the plane do not change with the excitation amplitude or the energy in the system.

For the vertical direction, the IWD analysis results in four components corresponding to modes 1, 2, 4, and 6; however, just as in the computational study, we consider only the first and sixth modes in the analysis presented here. The justification for this is the same as in the computational study, which is that if the 2D-NVA is effective at mitigating the sixth mode, which has the highest frequency of the modes considered in this study, then it will also mitigate the second and fourth modes. To this end, we depict the original displacement time series and the time series for the first and sixth modes in Fig. 18a, b, and c for 50, 165, and 250 N, respectively, for all three configurations. In all three forcing cases, the amplitudes of the first and sixth modes of the plane with the 2D-NVAs installed are substantially smaller than those for the plane without any 2D-NVAs installed, except for the response of mode 6 for 165 N with two active 2D-NVAs. The response of mode 6 for 165 N with two active 2D-NVAs depicts a strong beating pattern, which implies a strong transfer of energy into that mode facilitated by the impacts of the 2D-NVA. The maximum absolute displacements for each mode for each configuration and forcing is provided in Table 7 along with the percent difference using the plane with no NVAs as the baseline. On average, the 2D-NVAs reduce the maximum amplitude of the first mode across all forcing levels by 75.0% and 70.0% for the configurations with one and two active 2D-NVAs, respectively. The 2D-NVAs reduce the maximum amplitude of the sixth mode by 63.7% and 51.0% for one and two active NVAs, respectively. Interestingly, we find that the performance of only a single active 2D-NVA is better than that for two active 2D-NVAs. However, as seen with the vertical direction, both configurations result in a substantial reduction in the amplitude of both modes.

For the longitudinal direction, the IWD analysis results in two components corresponding to modes 3 and 5, and we consider both modes in the analysis presented here. To this end, we depict the original displacement time series and the time series for the third and fifth modes in Fig. 19a, b, and c for 50, 165, and 250 N, respectively, for all three configurations. In all three forcing cases, the amplitudes of the third and sixth modes with the 2D-NVAs installed are substantially lower than those for the plane without any 2D-NVAs installed. The maximum absolute displacements for each mode for each configuration and forcing is provided in Table 8 along with the percent difference using the plane with no NVAs as the baseline. On average, the 2D-NVAs reduce the maximum amplitude of the third mode across all forcing levels by 64.4% and 89.7% for the configurations with one and two active 2D-NVAs,

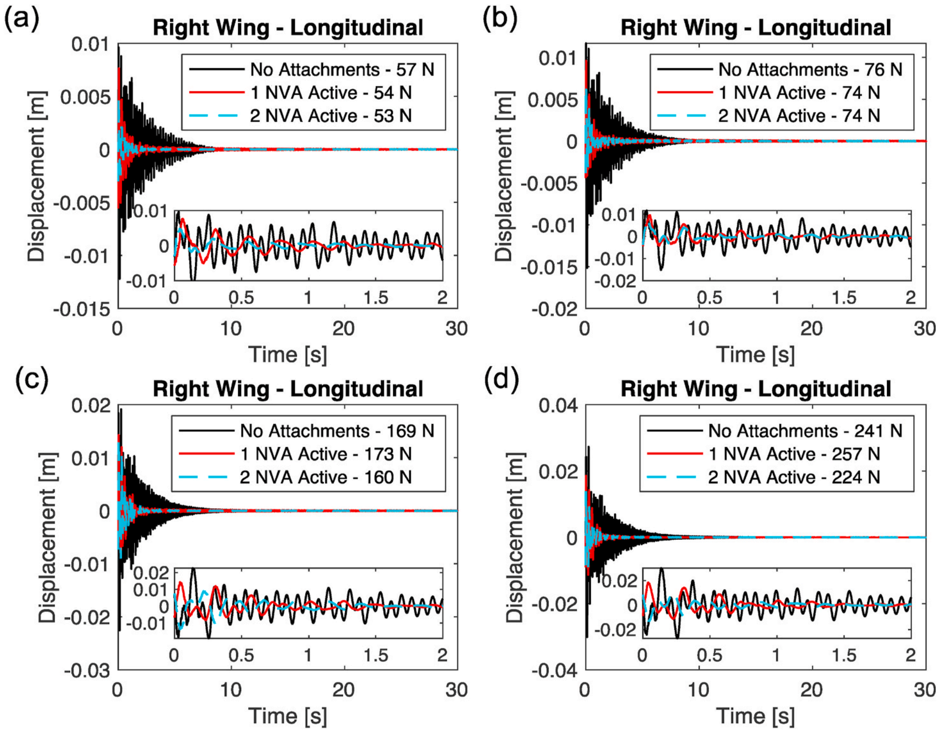

Fig. 16. The longitudinal response of the right wingtip for the three configurations under impulsive excitation in the longitudinal direction with nominal amplitude of (a) 50 N, (b), 76 N, (c) 155 N, and (d) 280 N.

Table 5
The 5% settling times for longitudinal response under longitudinal excitation.

Force [N]	No NVAs	One 2D-NVA Active		Two 2D-NVAs Active	
	Time [s]	Time [s]	Percent Reduction [%]	Time [s]	Percent Reduction [%]
50	10.17	3.96	61.1	3.81	62.5
75	9.86	3.9	60.4	4.35	55.9
165	9.08	3.89	57.2	3.37	62.9
250	9.1	2.66	70.8	3.08	66.2
Average	**9.55**	**3.60**	**62.4**	**3.65**	**61.9**

respectively. The 2D-NVAs reduce the maximum amplitude of the sixth mode by 56.4% and 75.3% for one and two active NVAs, respectively. Unlike the vertical direction, we find that the performance of two active 2D-NVA is significantly better than that for only one active 2D-NVAs; however, both configurations result in a substantial reduction in the amplitude of both modes.

5. Concluding remarks

This research considered the performance of a novel two-dimensional nonlinear vibration absorber (2D-NVA) for mitigating the motion of a model commercial aircraft with HAR-wings in both the vertical and longitudinal directions simultaneously. The effectiveness of the 2D-NVA system was investigated computationally using a finite element model for the HAR-wing aircraft with one active and one inactive 2D-NVA. The computational results showed that the proposed 2D-NVA is suitable for mitigating the motion of the airplane in both longitudinal and vertical directions simultaneously. The results demonstrated a significant reduction in the 5% settling times across a wide range of forcing angles and amplitudes. A further investigation into the response of the vertical and longitudinal modes was performed by extracting each mode using the IWD method. The results of this analysis revealed that the 2D-NVA can mitigate the motion of the plane by both transferring energy from low frequencies to high frequencies and by irreversibly absorbing the energy from multiple modes simultaneously.

The experimental study investigated the performance of both one active and two active 2D-NVAs using a model HAR-wing aircraft that was comparable to the one used in the computational study. The experimental system was excited in only one direction at a time and four forcing cases were considered in each direction for all three configurations. The performance of the 2D-NVAs was investigated by considering the reduction in 5% settling time and maximum displacement amplitude of the two configurations with active 2D-NVAs to those for the configuration with no 2D-NVAs installed at all. The effect of the 2D-NVAs on the modes of the plane were investigated using the same IWD analysis as

Table 6
The maximum displacements for longitudinal response under longitudinal excitation.

Force [N]	No NVAs	One 2D-NVA Active		Two 2D-NVAs Active	
	Displacement [mm]	Displacement [mm]	Percent Reduction [%]	Displacement [mm]	Percent Reduction [%]
50	12.21	7.63	37.5	4.96	59.4
75	15.16	9.57	36.9	6.49	57.2
165	22.58	14.30	36.7	13.94	38.3
250	30.10	18.53	38.4	13.90	53.8
Average	-	-	**37.4**	-	**52.2**

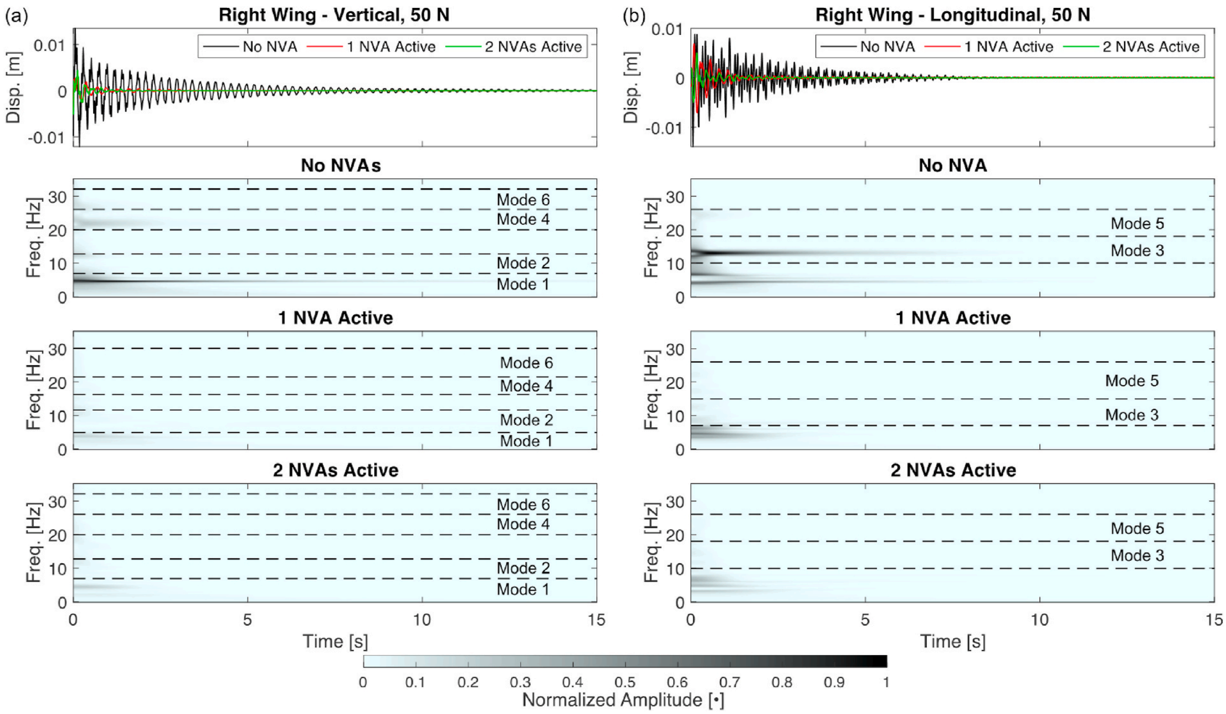

Fig. 17. Comparison of the displacement response and corresponding CWT spectra of the left-wing tip for 50 N for (a) the vertical direction and (b) the longitudinal direction.

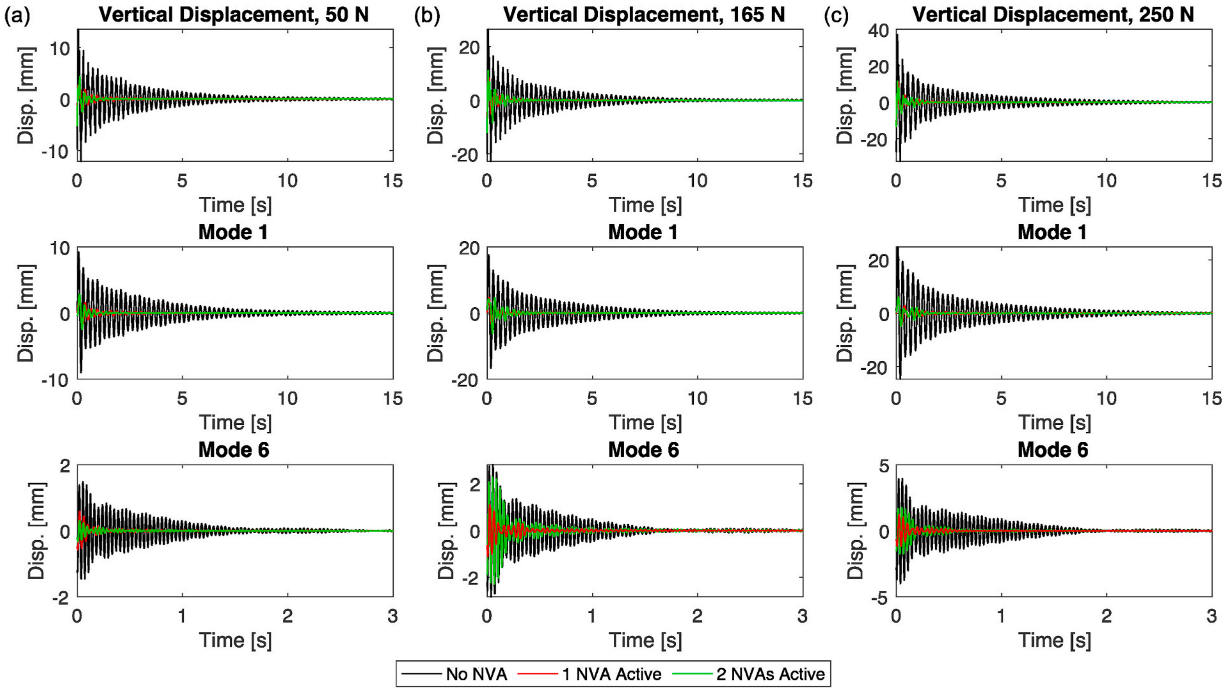

Fig. 18. The displacement response of the right-wing tip in the vertical direction and the responses of modes 1 and 6 for nominal forcing amplitudes of (a) 50 N, (b) 155 N, and (c) 280 N.

in the computational study. The results demonstrated that one active 2D-NVA is optimal for mitigating the motion of the plane in the vertical direction, while two active 2D-NVAs is optimal for the longitudinal direction. The analysis also demonstrated that the 2D-NVA system is robust to changes in the frequency content of the parent structure.

The proposed 2D-NVA system could have applications in other areas, such as the seismic response of buildings or multi-dimensional vibrations of drill strings. Future research efforts will focus on 1) optimizing the housing cavity to improve the performance of the 2D-NVA system across multiple directions and 2) investigating the performance of the 2D-NVA under aeroelastic loading for applications in flutter suppression.

Table 7
The maximum displacements for modes 1 and 6 under vertical excitation.

Mode	Force [N]	No NVAs	One 2D-NVA Active		Two 2D-NVAs Active	
		Displacement [mm]	Displacement [mm]	Percent Reduction [%]	Displacement [mm]	Percent Reduction [%]
1	50	9.25	2.21	76.1	2.84	69.3
	165	17.6	4.75	73.1	6.20	64.8
	250	24.8	5.99	75.8	6.00	75.8
6	50	1.48	0.58	60.8	0.33	77.7
	165	2.83	1.11	60.7	2.28	19.4
	250	4.01	1.21	69.7	1.77	55.8

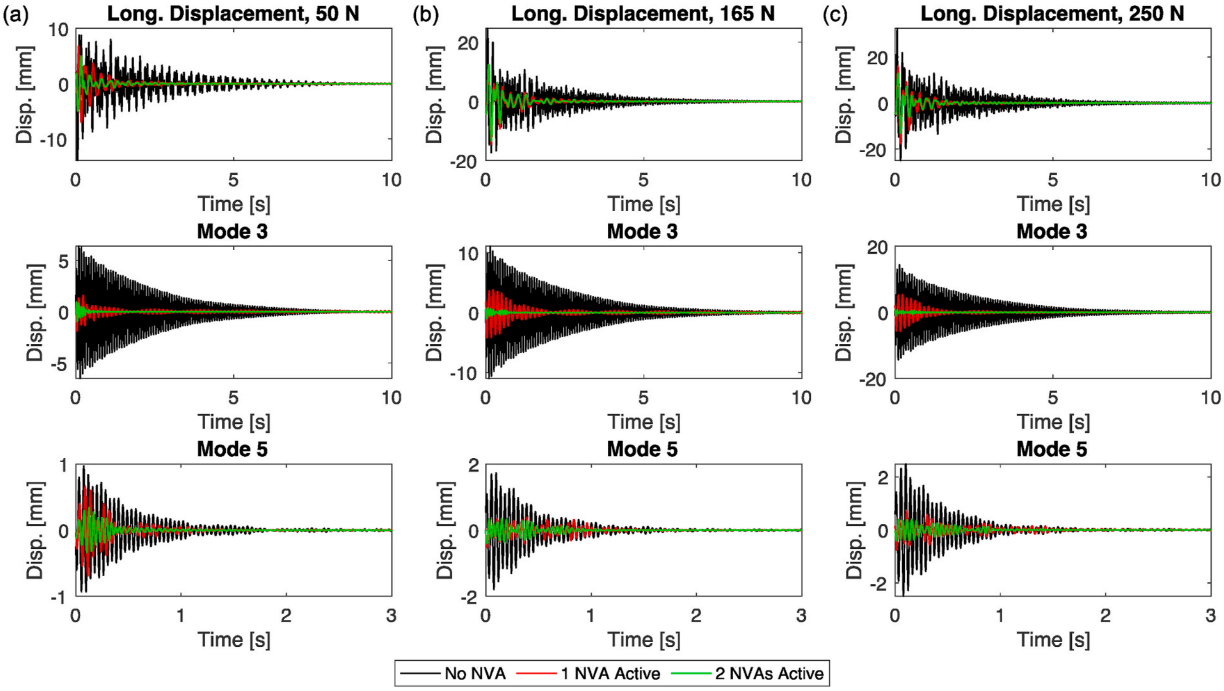

Fig. 19. The displacement response of the right-wing tip in the longitudinal direction and the responses of modes 3 and 5 for nominal forcing amplitudes of (a) 50 N, (b) 155 N, and (c) 280 N.

Table 8
The maximum displacements for modes 3 and 5 under longitudinal excitation.

Mode	Force [N]	No NVAs	One 2D-NVA Active		Two 2D-NVAs Active	
		Displacement [mm]	Displacement [mm]	Percent Reduction [%]	Displacement [mm]	Percent Reduction [%]
3	50	6.50	1.89	70.8	0.96	85.3
	165	11.1	4.22	61.9	1.00	91.0
	250	14.4	5.70	60.4	1.05	92.7
5	50	0.97	0.69	28.9	0.35	64.4
	165	1.79	0.52	70.7	0.40	77.8
	250	2.50	0.76	69.5	0.41	83.7

Declarations

The authors declare that there are no conflicts of interest or competing interests regarding the publication of this article.

Funding

This research was supported by the NASA Nebraska Space Grant (Federal Award #NNX15AI09H), the NASA Nebraska EPSCoR Research Infrastructure Development (RID) Program FY2019-2021 (Federal Award #80NSSC19M0065), and by the National Science Foundation Disabilities and Rehabilitation Engineering Program under award number 2203144. The authors are grateful for this funding.

Data availability

The datasets generated during and/or analyzed during the current study are available from the corresponding author on reasonable request.

CRediT authorship contribution statement

Judith D. Brown: Data curation, Formal analysis, Investigation, Software, Validation, Writing – original draft, Writing – review & editing. **Manal Mustafa:** Data curation, Formal analysis, Investigation, Validation, Writing – original draft, Writing – review & editing. **Keegan J. Moore:** Conceptualization, Data curation, Formal analysis, Funding acquisition, Investigation, Methodology, Project administration, Resources, Software, Supervision, Validation, Visualization, Writing – original draft, Writing – review & editing.

Declaration of competing interest

The authors declare the following financial interests/personal relationships which may be considered as potential competing interests:

Keegan Moore reports financial support was provided by Nebraska Space Grant Consortium. Keegan Moore reports financial support was provided by National Science Foundation.

Data availability

Data will be made available on request.

Acknowledgements

This work was completed utilizing the Holland Computing Center of the University of Nebraska, which receives support from the Nebraska Research Initiative.

References

[1] N.T. Nguyen, J. Fugate, U.K. Kaul, J. Xiong, Flutter analysis of the transonic truss-braced wing aircraft using transonic correction, in: AIAA Scitech 2019 Forum, American Institute of Aeronautics and Astronautics, 2019, https://doi.org/10.2514/6.2019-0217.

[2] N.A. Harrison, G.M. Gatlin, S.A. Viken, M. Beyar, E.D. Dickey, K. Hoffman, E. Y. Reichenbach, Development of an efficient M=0.80 transonic truss-braced wing aircraft, in: AIAA Scitech 2020 Forum, American Institute of Aeronautics and Astronautics, 2020, https://doi.org/10.2514/6.2020-0011.

[3] J. Ormondroyd, J. Den Hartog, The theory of the dynamic vibration absorber, Trans. ASME J. Appl. Mech. 50 (1928) 9–22.

[4] L. Koutsoloukas, N. Nikitas, P. Aristidou, Passive, semi-active, active and hybrid mass dampers: a literature review with associated applications on building-like structures, Developments in the Built Environment 12 (2022) 100094, https://doi.org/10.1016/j.dibe.2022.100094.

[5] J.F. Vignola, J.A. Judge, A.J. Kurdila, Shaping of a system's frequency response using an array of subordinate oscillators, J. Acoust. Soc. Am. 126 (2009) 129–139, https://doi.org/10.1121/1.3143783.

[6] J. Sterling, J. Vignola, J. Gietl, T. Ryan, N. Sonne, S.T. Paruchuri, Effect of increased damping in subordinate oscillator arrays, J. Phys. Conf. Ser. 1149 (2018) 012006, https://doi.org/10.1088/1742-6596/1149/1/012006.

[7] J. Sterling, S.T. Paruchuri, T.J. Ryan, J. Vignola, A.J. Kurdila, Subordinate oscillator arrays: physical design and effects of error, Engrxiv.Org, https://engrxiv.org/preprint/view/924, 2020. (Accessed 16 June 2023).

[8] A.F. Vakakis, Passive nonlinear targeted energy transfer, Phil. Trans. Roy. Soc. Lond.: Math. Phys. Eng. Sci. 376 (2018) 20170132, https://doi.org/10.1098/rsta.2017.0132.

[9] A.F. Vakakis, O.V. Gendelman, L.A. Bergman, A. Mojahed, M. Gzal, Nonlinear targeted energy transfer: state of the art and new perspectives, Nonlinear Dynam. (2022), https://doi.org/10.1007/s11071-022-07216-w.

[10] Y. Starosvetsky, O.V. Gendelman, Vibration absorption in systems with a nonlinear energy sink: nonlinear damping, J. Sound Vib. 324 (2009) 916–939, https://doi.org/10.1016/j.jsv.2009.02.052.

[11] Y. Liu, G. Chen, X. Tan, Dynamic analysis of the nonlinear energy sink with local and global potentials: geometrically nonlinear damping, Nonlinear Dynam. 101 (2020) 2157–2180, https://doi.org/10.1007/s11071-020-05876-0.

[12] Y. Zhang, X. Kong, C. Yue, H. Xiong, Dynamic analysis of 1-dof and 2-dof nonlinear energy sink with geometrically nonlinear damping and combined stiffness, Nonlinear Dynam. 105 (2021) 167–190, https://doi.org/10.1007/s11071-021-06615-9.

[13] Y. Bichiou, M.R. Hajj, A.H. Nayfeh, Effectiveness of a nonlinear energy sink in the control of an aeroelastic system, Nonlinear Dynam. 86 (2016) 2161–2177. https://link-springer-com.proxy2.library.illinois.edu/article/10.1007/s11071-016-2922-y. (Accessed 26 July 2017).

[14] D.R.Q. Pacheco, F.D. Marques, A.J.M. Ferreira, Panel flutter suppression with nonlinear energy sinks: numerical modeling and analysis, Int. J. Non Lin. Mech. 106 (2018) 108–114, https://doi.org/10.1016/j.ijnonlinmec.2018.08.009.

[15] T. Yang, S. Hou, Z.-H. Qin, Q. Ding, L.-Q. Chen, A dynamic reconfigurable nonlinear energy sink, J. Sound Vib. 494 (2021) 115629, https://doi.org/10.1016/j.jsv.2020.115629.

[16] D.-D. Tan, Z.-Q. Lu, D.-H. Gu, H. Ding, L.-Q. Chen, A ring vibration isolator enhanced by a nonlinear energy sink, J. Sound Vib. 508 (2021) 116201, https://doi.org/10.1016/j.jsv.2021.116201.

[17] J. Zhou, M. Xu, J. Zha, Z. Yang, The suppression of nonlinear panel flutter response at elevated temperatures using a nonlinear energy sink, Meccanica 56 (2021) 41–57, https://doi.org/10.1007/s11012-020-01269-0.

[18] A. Singh, K.J. Moore, Identification of multiple local nonlinear attachments using a single measurement case, J. Sound Vib. 513 (2021) 116410, https://doi.org/10.1016/j.jsv.2021.116410.

[19] C. Wang, E.J. Krings, A.T. Allen, E.J. Markvicka, K.J. Moore, Low-to-High frequency targeted energy transfer using a nonlinear energy sink with softening-hardening nonlinearity, Int. J. Non Lin. Mech. (2022), https://doi.org/10.1016/j.ijnonlinmec.2022.104194.

[20] F. Nucera, A.F. Vakakis, D.M. McFarland, L.A. Bergman, G. Kerschen, Targeted energy transfers in vibro-impact oscillators for seismic mitigation, Nonlinear Dynam. 50 (2007) 651–677, https://doi.org/10.1007/s11071-006-9189-7.

[21] I. Karayannis, A.F. Vakakis, F. Georgiades, Vibro-impact attachments as shock absorbers, Proc. Inst. Mech. Eng. Part C 222 (2008) 1899–1908, https://doi.org/10.1243/09544062JMES864.

[22] T. Li, E. Gourc, S. Seguy, A. Berlioz, Dynamics of two vibro-impact nonlinear energy sinks in parallel under periodic and transient excitations, Int. J. Non Lin. Mech. 90 (2017) 100–110. http://www.sciencedirect.com/science/article/pii/S0020746216302220.

[23] J. Wang, B. Wang, Z. Liu, H. Li, C. Zhang, Seismic response mitigation of building structures with a novel vibro-impact dual-mass damper, Eng. Struct. 215 (2020) 110673, https://doi.org/10.1016/j.engstruct.2020.110673.

[24] M.A. AL-Shudeifat, A.S. Saeed, Comparison of a modified vibro-impact nonlinear energy sink with other kinds of NESs, Meccanica 56 (2021) 735–752, https://doi.org/10.1007/s11012-020-01193-3.

[25] H. Li, A. Li, Y. Zhang, Importance of gravity and friction on the targeted energy transfer of vibro-impact nonlinear energy sink, Int. J. Impact Eng. 157 (2021) 104001, https://doi.org/10.1016/j.ijimpeng.2021.104001.

[26] J. Wang, C. Zhang, Y. Zheng, A novel mass damper enabled by three types of mass attachments and internal vibro impacts, J. Sound Vib. 534 (2022) 117065, https://doi.org/10.1016/j.jsv.2022.117065.

[27] J. Wang, C. Zhang, H. Li, Z. Liu, A vertical-vibro-impact-enhanced track bistable nonlinear energy sink for robust and comprehensive control of structures, Struct. Control Health Monit. (2022), https://doi.org/10.1002/stc.2931.

[28] S. Li, H. Wu, J. Chen, Global dynamics and performance of vibration reduction for a new vibro-impact bistable nonlinear energy sink, Int. J. Non Lin. Mech. 139 (2022) 103891, https://doi.org/10.1016/j.ijnonlinmec.2021.103891.

[29] O.V. Gendelman, Targeted energy transfer in systems with non-polynomial nonlinearity, J. Sound Vib. 315 (2008) 732–745, https://doi.org/10.1016/j.jsv.2007.12.024.

[30] M.A. AL-Shudeifat, Nonlinear energy sinks with piecewise-linear nonlinearities, J. Comput. Nonlinear Dynam. 14 (2019), https://doi.org/10.1115/1.4045052.

[31] H. Yao, Y. Cao, S. Zhang, B. Wen, A novel energy sink with piecewise linear stiffness, Nonlinear Dynam. 94 (2018) 2265–2275, https://doi.org/10.1007/s11071-018-4488-3.

[32] H. Yao, Y. Cao, Y. Wang, B. Wen, A tri-stable nonlinear energy sink with piecewise stiffness, J. Sound Vib. 463 (2019) 114971, https://doi.org/10.1016/j.jsv.2019.114971.

[33] A. Singh, K.J. Moore, Characteristic nonlinear system identification of local attachments with clearance nonlinearities, Nonlinear Dynam. (2020), https://doi.org/10.1007/s11071-020-06004-8.

[34] J.E. Chen, M. Sun, W.H. Hu, J.H. Zhang, Z.C. Wei, Performance of non-smooth nonlinear energy sink with descending stiffness, Nonlinear Dynam. 100 (2020) 255–267, https://doi.org/10.1007/s11071-020-05528-3.

[35] M.A. Al-Shudeifat, A.S. Saeed, Periodic motion and frequency energy plots of dynamical systems coupled with piecewise nonlinear energy sink, J. Comput. Nonlinear Dynam. 17 (2022), https://doi.org/10.1115/1.4053509.

[36] W. Tian, Y. Li, P. Li, Z. Yang, T. Zhao, Passive control of nonlinear aeroelasticity in hypersonic 3-D wing with a nonlinear energy sink, J. Sound Vib. 462 (2019) 114942, https://doi.org/10.1016/j.jsv.2019.114942.

[37] W. Tian, Y. Li, Z. Yang, P. Li, T. Zhao, Suppression of nonlinear aeroelastic responses for a cantilevered trapezoidal plate in hypersonic airflow using an energy harvester enhanced nonlinear energy sink, Int. J. Mech. Sci. 172 (2020) 105417, https://doi.org/10.1016/j.ijmecsci.2020.105417.

[38] W. Tian, T. Zhao, Y. Gu, Z. Yang, Nonlinear flutter suppression and performance evaluation of periodically embedded nonlinear vibration absorbers in a supersonic FGM plate, Aero. Sci. Technol. 121 (2022) 107198, https://doi.org/10.1016/j.ast.2021.107198.

[39] A.S. Saeed, M.A. AL-Shudeifat, W.J. Cantwell, A.F. Vakakis, Two-dimensional nonlinear energy sink for effective passive seismic mitigation, Commun. Nonlinear Sci. Numer. Simul. 99 (2021) 105787, https://doi.org/10.1016/j.cnsns.2021.105787.

[40] C. Wang, J.D. Brown, A. Singh, K.J. Moore, A two-dimensional nonlinear vibration absorber using elliptical impacts and sliding, Mech. Syst. Signal Process. 189 (2023) 110068, https://doi.org/10.1016/j.ymssp.2022.110068.

[41] A. Mojahed, L.A. Bergman, A.F. Vakakis, New inverse wavelet transform method with broad application in dynamics, Mech. Syst. Signal Process. 156 (2021) 107691, https://doi.org/10.1016/j.ymssp.2021.107691.

[42] C.M. Roithmayr, Relating Constrained Motion to Force through Newton's Second Law, Ph.D., Georgia Institute of Technology, 2007. https://smartech.gatech.edu/bitstream/handle/1853/14592/roithmayr_carlos_m_200705_phd.pdf?sequence=1&isAllowed=y.

[43] C.M. Roithmayr, D.H. Hodges, Forces associated with non-linear non-holonomic constraint equations, Int. J. Non Lin. Mech. 45 (2010) 357–369, https://doi.org/10.1016/j.ijnonlinmec.2009.12.009.

[44] D.J. Ewins, Modal Testing: Theory, Practice, and Application, Research Studies Press, 2000.

[45] Saang Bum Kim, B.F. Spencer, Yun Chung-Bang, Frequency domain identification of multi-input, multi-output systems considering physical relationships between measured variables, J. Eng. Mech. 131 (2005) 461–472, https://doi.org/10.1061/(ASCE)0733-9399(2005)131:5461.
[46] M.H. Richardson, D.L. Formenti, Parameter Estimation from Frequency Response Measurements Using Rational Fraction Polynomials, 1982. Orlando, FL.
[47] Slippery Delrin® acetal AF Resin disc, McMaster-carr (n.d.), https://www.mcmaster.com/9969K21/. (Accessed 19 February 2024).
[48] H. King, R. White, I. Maxwell, N. Menon, Inelastic impact of a sphere on a massive plane: nonmonotonic velocity-dependence of the restitution coefficient, EPL 93 (2011) 14002, https://doi.org/10.1209/0295-5075/93/14002.
[49] P.S. Addison, The Illustrated Wavelet Transform Handbook Introductory Theory and Applications in Science, Engineering, Medicine and Finance, Taylor & Francis, New York, 2002.
[50] K.J. Moore, A. Mojahed, L.A. Bergman, A.F. Vakakis, Local nonlinear stores induce global effects in the dynamics of an experimental model airplane, AIAA J. 57 (2019) 4953–4965, https://doi.org/10.2514/1.J058311.